

**Single-Particle Production
and Photon-Hadron Correlations
in $p + p$ Collisions
at Next-to-Leading-Order**

Jonathan COULL

Department of Physics,

McGill University, Montreal, Canada

`jonathan.coull@mail.mcgill.ca`

June 2011

A thesis submitted to McGill University in partial fulfillment of the requirements of the degree of Master's of Science.

©Jonathan Coull 2011

Abstract

In this thesis, we study photon production and photon-hadron correlations at next-to-leading order (NLO) in proton-proton collisions, in both the cases of isolated and non-isolated photons. To begin, fundamentals of perturbative Quantum Chromodynamics (pQCD) are reviewed, with an emphasis on describing how to compute spectra for single particle production and correlated pairs at both leading order (LO) and NLO in hadronic collisions. In particular, a discussion of infrared and collinear singularities at NLO will provide a natural introduction to the concept of factorization. These results are then specifically applied to the case of computing photon and pion single-particle cross-sections in proton-proton collisions at Relativistic Heavy-Ion Collider (RHIC) and Large Hadron Collider (LHC) energies, and compared to experimental data from the PHENIX and CMS experiments respectively. Included in this will be a short study of the theoretical systematic uncertainty generated by the dependence on factorization scales, and a discussion of the modifications needed when moving from inclusive to isolated observables. Following this, double inclusive cross-sections for production of photon-tagged hadrons are computed and compared to data from PHENIX. Once again, a full NLO treatment is given, and the effects of isolation are implemented. We will conclude with a final section on the application of photon-hadron correlations to the tomographic mapping of energy loss in heavy-ion collisions.

Résumé

Dans cette dissertation, nous étudions la production au seconde ordre (NLO) de photons ainsi que la corrélation entre photons durs et hadrons dans les collisions proton-proton. Dans les deux cas est inclus l'effet de l'application de critères d'isolement sur les photons. Nous commençons par une synthèse des résultats fondamentaux de la chromodynamique quantique perturbative (pQCD), dans laquelle nous résumons les méthodes principales pour calculer des sections efficaces aux premier et second ordres. En particulier, nous discutons des singularités infrarouges et colinéaires qui se produisent au seconde ordre, ce qui nous amènera à introduire la théorie de la factorisation. Ces outils sont par la suite utilisés pour calculer les section efficaces pour la production de photons et de pions dans les collisions proton-proton aux énergies atteintes au *Relativistic Heavy Ion Collider* (RHIC) et au Grand collisionneur de hadrons (LHC). Ces résultats sont comparés aux données des expériences PHENIX et CMS respectivement. Nous étudions aussi l'incertitude théorique due aux choix des échelles de factorisation et la différence entre les sections efficaces inclusives et isolées. Finalement, nous calculons les sections efficaces pour les paires photon-hadron corrélées et comparons les résultats aux données de PHENIX, tout en incluant les effets de second ordre et d'isolement. Nous concluons avec une description qualitative de l'application des corrélations pour établir une tomographie des collisions d'ions lourds.

Contents

Abstract	1
Résumé	1
Acknowledgements	5
Notation and Units	6
1 Introduction	7
1.1 The Standard Model	7
1.2 The Importance of Collider Physics	8
1.3 Photon Production and Photon-Hadron Correlations	9
1.4 Next-to-leading Order Computations	11
1.5 Outline of Thesis	12
2 Perturbative QCD	14
2.1 Introduction	14
2.2 Cross-sections	15
2.3 pQCD Processes	18
2.3.1 Leading-order amplitudes	18
2.3.2 Divergences at Next-to-leading order	20
2.4 Asymptotic Freedom and Color Confinement	22
2.4.1 The running of the coupling constants	22
2.4.2 Color Confinement	25
2.5 The Factorization Theorem	26
2.5.1 Introduction	26
2.5.2 Factorization in photon production	28

2.5.3	Fitting PDFs and FFs	30
2.5.4	Scale Dependences	31
2.6	Hadronic Kinematics	33
2.6.1	Leading order	33
2.6.2	Next-to-leading order	36
3	Photon Production	38
3.1	Introduction	38
3.2	Leading-Order Photon Production	39
3.2.1	Computing the LO cross-section	39
3.2.2	Modifying our scale dependences	42
3.3	NLO Photon Production	44
3.4	Isolation Criteria	48
3.4.1	Introduction	48
3.4.2	Isolated fragmentation photons	49
3.4.3	Isolated direct photons	51
3.4.4	Results	53
3.5	Hadron Production	55
4	Photon-Hadron Correlations	58
4.1	Introduction	58
4.2	Leading-order Photon-pion Cross-section	59
4.3	NLO Cross-section	61
4.3.1	NLO Observables	61
4.3.2	Isolation revisited	63
4.3.3	Results	65
4.4	Applications to Nucleus-Nucleus Collisions	67
5	Conclusion	73
A	QCD Feynman Rules	76

List of Figures

2.1	The only tree-level Feynman diagram contributing to the process $q + q' \rightarrow q + q'$	19
2.2	Possible tree-level Feynman diagrams for the process $q + q' \rightarrow \gamma + q + q'$. 20	
2.3	α_s plotted at LO and NLO as a function of the energy scale μ	25
2.4	A heuristic illustration of color confinement.	26
2.5	A schematic of the collision of two hadrons A and B , the ensuing partonic interaction $ab \rightarrow cd$, and final-state fragmentation of jets into observed hadrons.	27
2.6	A heuristic depiction of how the singularities in $qq \rightarrow qq\gamma$ are factorized and absorbed into the relevant distribution functions.	30
2.7	A schematic of the collision of two hadrons A and B , the ensuing partonic interaction $ab \rightarrow cd$, and final-state production of a fragmentation photon γ and a jet d	34
3.1	LO partonic processes for photon production.	40
3.2	LO high- p_T photon spectrum in pp collisions at $\sqrt{s} = 200\text{GeV}$	41
3.3	LO high- p_T photon spectrum in pp collisions at RHIC, calculated at various scales, and the corrective factor due to modifying these scales.	43
3.4	A few examples of real and virtual NLO photon production diagrams. 45	
3.5	NLO “direct” γ production vs. LO “fragmentation” γ production.	46
3.6	NLO High- p_T photon spectrum in pp collisions at $\sqrt{s} = 200\text{GeV}$	47
3.7	K -factors for photon production in the kinematic range $4\text{GeV} < p_T^\gamma < 15\text{GeV}$	48

3.8	A schematic of how final-state hadronic energy may originate from the fragmentation process at LO (left), and from extra final-state partons at NLO (right).	50
3.9	High- p_T isolated photon spectrum in pp collisions at $\sqrt{s} = 7TeV$	54
3.10	High- p_T isolated photon spectrum in pp collisions at $\sqrt{s} = 7TeV$, calculated at NLO, with scales set to $\mu = Q = Q_F = 2p_T^\gamma$	55
3.11	High- p_T pion spectrum in pp collisions at RHIC, calculated at LO and NLO. The data points and error bars are taken from PHENIX.[58] $\mu = Q = Q_F = p_T^\pi$. The bottom subfigure gives the K -factor.	56
4.1	The LO away-side charged hadron yield per isolated direct photon trigger as a function of z for the ranges $5 < p_T^{trig} < 7GeV/c$, $7 < p_T^{trig} < 9GeV/c$, and $9 < p_T^{trig} < 12GeV/c$	60
4.2	The LO away-side charged hadron yield per direct photon trigger as a function of z for various p_T^γ bins at the LHC.	62
4.3	Invariant mass distribution for $\gamma - \pi_0$ pairs in the $80 - 140GeV$ range at $\sqrt{s} = 14TeV$, with isolation criteria $R = 0.4$ and varying E_T^{max}	64
4.4	Invariant mass distribution for $\gamma - \gamma$ pairs in the $80 - 140GeV$ range at $\sqrt{s} = 14TeV$, with isolation criteria $R = 0.4$ and varying E_T^{max}	66
4.5	The NLO away-side charged hadron yield per isolated photon trigger as a function of x_E for the ranges $5 < p_T^{trig} < 7GeV/c$, $7 < p_T^{trig} < 9GeV/c$, and $9 < p_T^{trig} < 12GeV/c$	68
4.6	The NLO away-side charged hadron yield per isolated photon trigger as a function of x_E for the range $85 < p_T^{trig} < 120GeV/c$ at LHC energies.	69
4.7	High- p_T pion R_{AA} in Au+Au collisions, as measured by PHENIX.[14] 70	
4.8	High- p_T pion R_{AA} in Au+Au collisions. The diagram is taken from [74].	71
A.1	Propagator rules in QCD	78
A.2	Vertex rules in QCD	79
A.3	Quark-photon vertex	80

Acknowledgements

I'd like to express an immense amount of gratitude to my thesis supervisor Prof. Charles Gale for invaluable support and mentorship over the past two years. He has played an immeasurable role in guiding me to this research topic, honing my ideas into the stuff of an interesting and complete thesis, and providing continual academic and moral support throughout the journey. It is safe to say that the knowledge imparted in these pages is as much his as it is mine.

I am grateful to the other professors and researchers in the nuclear theory group, who have contributed in constructing a stimulating, challenging environment for me at McGill. Particular thanks is owed to my colleague Jean-François Pacquet, with whom countless discussions have helped clarify a great many of the topics presented here. His unrelenting willingness to answer my inane questions about computer programming have saved me uncountable hours of frustration.

Special thanks is owed to Prof. Jean-Philippe Guillet of the Laboratoire de physique théorique d'Annecy le vieux, who provided me with valuable help in troubleshooting issues with the PHOX programs.

I would be remiss not to thank Hydro-Québec, who have graciously provided me with funding for the past two years under their MSc bursary program. This has been an invaluable source of financial support and I'm tremendously humbled and grateful to have benefited by it.

Finally, I could not have made it the past couple of years without the support of my family and friends, without whom endeavours such as this could not hold much meaning. The things that we learn about ourselves in life don't come from equations staring up from a page, but from the relationships and human bonds whose complexity and beauty no theory could adequately contain. It is in these shared bonds that we are able to discover our own compassionate natures, and so begin to strive for greatness.

Notation and Units

So that consistent notation is used throughout the entire thesis, we mention the important conventions that are used. The metric for Minkowski space-time is given by:

$$\eta_{\mu\nu} = \begin{pmatrix} 1 & 0 & 0 & 0 \\ 0 & -1 & 0 & 0 \\ 0 & 0 & -1 & 0 \\ 0 & 0 & 0 & -1 \end{pmatrix} \quad (1)$$

Three-vectors will be denoted by boldface (e.g.: \mathbf{p}) while four-vectors will be denoted with greek indices (p^μ) or in plain type (p) when the context is clear. As usual, slash notation is just defined as $\not{p} = \gamma_\mu p^\mu$.

The Einstein summation convention is employed. If indices are both subscript or both superscript (e.g.: for flavor or color indices), the sum is to be done in Euclidean metric; if one index is subscript and the other superscript (this will only occur for Lorentz indices) the sum is to be done in Minkowskian metric.

We make use of the system of natural units in which $\hbar = c = k_b = 1$ for most of our calculations. The units will often be subtly restored when comparing theoretical results to experimental data given in SI units. While we denote the strong coupling constant as α_s , we denote the electromagnetic coupling as α , without any subscript.

When there are variables that are defined for both the hadronic and partonic case (e.g.: the Mandelstam variables s, t, u), we will denote the latter with a caret (\hat{s} for hadronic process, \hat{s} for partonic process).

Finally, Feynman diagrams are always drawn with the time direction extending from left to right.

Chapter 1

Introduction

1.1 The Standard Model

The goal of small-distance physics today is incredibly broad and far-reaching: We seek to have a complete picture of no less than the entire set of fundamental constituents that make up the universe, and the interactions between these constituents. While, for a long time, the experimental energies necessary for exploring the desired regimes was simply not attainable, the advent of a new generation of particle colliders – most recently the Large Hadron Collider (LHC) – has provided a new testing ground for this area of physics.

The current accepted model to which data is compared is known as the *Standard Model* of particle physics [1, 2, 3], which provides a description of the electromagnetic force as well as both the weak and strong nuclear forces. Though much of high-energy physics today is centered around the belief that the Standard Model (SM) is merely part of a larger physical framework, such as string theory or other models that incorporate supersymmetry, there are very few contradictions between the model’s predictions and the vast majority of available data.

The SM is a quantum field theory described by the gauge group $SU_C(3) \otimes SU_W(2) \otimes U_Y(1)$, in which the $SU_C(3)$ group *Quantum Chromodynamics* (QCD) describes the strong nuclear force, and the $SU_W(2) \otimes U_Y(1)$ theory describes the electroweak force. The matter content of QCD consists of spin- $\frac{1}{2}$ particles called *quarks and antiquarks*, whose existence was first proposed in the earlier Quark Model [4, 5], while the strong force is mediated by gauge bosons known as *gluons*.

Because in this thesis we only deal with problems involving the physical interactions of hadrons and nuclei, which are entirely composed of quarks and gluons, it is principally the interactions described by QCD that will be important for us. In addition, the interaction of photons with matter is described by the electromagnetic force, described by the $U_{em}(1)$ gauge theory *Quantum electrodynamics* (QED). This theory arises out of the spontaneous symmetry breaking process in the electroweak gauge theory, and, for our purposes, can be considered independently of the purely weak interactions.

1.2 The Importance of Collider Physics

Probing distances at the scale of interest requires particles that are energetic enough to “resolve” the physics at that scale. For the strong interaction, which has a range of $r \sim 1fm$, the uncertainty principle dictates that we need to be looking at particles with energies of the order $E \sim \frac{hc}{r} \sim 0.1 - 1 GeV$. To probe smaller distances requires yet high energies. The experimental fact is this : The only such particles that we are currently able to observe come from a) atmospheric phenomena, and b) colliders. The former offers a testing ground that, while attaining the necessary energies, is not a controllable setting in which specific reactions can be reproduced at will. Today’s particle colliders do have energy limitations, but offer a controlled setting to the experimentalist.

With regard to both proton-proton and nuclear collisions, the current state of the art is achieved at the Relativistic Heavy-Ion Collider (RHIC) at Brookhaven National Laboratory (BNL), which can accelerate proton pairs to a center-of-mass energy of 200 GeV , and the Large Hadron Collider (LHC) at the European Organization for Nuclear Research (CERN), which can achieve energies of 7 TeV . Although it only deals with hadronic collisions, the Fermilab Tevatron is able to accelerate both protons and anti-protons up to energies of 1 TeV .

Typical high-energy hadronic collisions produce a large number of final-state particles. At lower collision energies, the majority of produced particles have low transverse momenta – so-called “soft” collisions – while the higher p_T final states are generally the result of “hard” interactions between the hadronic constituents, which we know today to be quarks, antiquarks, and gluons. As one of these hard

final-state constituents propagates outward from the collision, the confining property of QCD (Section 2.4) will bring about the fragmentation and hadronization processes (Section 2.5), in which the parton transforms into a collimated "jet" of hadrons (and possibly other particles) that can be observed by the detector. This is generally accomplished through the use of calorimeters and spectrometers, which can, for example, differentiate particles based on charge, spin, mass and other properties.

Nuclear collisions offer a very different scenario. For heavy ions like gold or lead, there are sufficient degrees of freedom interacting so that the medium actually thermalizes, and we can apply a statistical mechanical treatment to the system. This allows for an experimental way of analyzing the phase diagram of QCD. In particular, the phase transition from a hadronic gas to a quark gluon plasma (QGP), predicted by lattice QCD models [6], was experimentally observed at RHIC several years ago [7] and is currently one of the most studied topics in high-energy nuclear physics.

Inversely related to the energy of the interaction is the time scale over which the interactions take place. When hadronic or nuclear collisions are performed, there is simply no time to send in external probes to analyze the system – the system can only be studied through the "probes" that it creates itself. In this light, what becomes important is the ability to define meaningful observables through these signatures, and determining what the observables have to say about the specific physical processes underlying each event.

1.3 Photon Production and Photon-Hadron Correlations

Because of the presence of a quark-photon interaction vertex in the SM, there is a source of hard photon production in both hadronic and nuclear collisions that arises directly from QCD interactions and which can therefore probe the strong interaction in a direct way. In the hadronic case, this observable can be exploited to constrain the gluon distribution of the proton at various energies [8], as well as being one of many processes that are able to put constraints on the value of the strong coupling α_s [9]. In the case of nuclear collisions, observing the thermal

photon signature – produced via soft interactions of the constituents of the thermal medium – in theory offers one way of measuring the temperature of the medium.

In both the hadronic and nuclear cases, there are multiple mechanisms of photon production, requiring careful calculations to take into account each individual signature. For example, in pp collisions, we observe “direct” hard photons originating from fundamental processes with a quark- γ vertex, as well as a contribution from the decay of long-lived mesons produced in the collision. In addition, it was shown in the mid-1980s that there was an additional source of production in which the photon acquired a “hadronic” structure and could actually fragment from an outgoing jet. The framework of the factorization theorem, outlined in Section 2.5, describes the theoretical relation between these two “direct” and “fragmentation” contributions.

In the case of nuclear collisions, we in addition observe photons originating from jet-medium interactions (“hard-soft” interactions) and thermal contributions (“soft-soft” interactions) from both the quark-gluon plasma phase and the hadronic phase. In light of the large number of production mechanisms, it is clear that having a good control over the “baseline” measurements obtained in pp collisions is a prerequisite for understanding the nuclear case.

Aside from the various applications of measuring single- γ spectra just mentioned, it turns out that two-particle spectra in which one or both particles are γ 's are very useful as well. A contemporary application has to do with the decay of the Higgs boson via $H \rightarrow \gamma\gamma$, which is expected to be a dominant channel at the LHC [10]. Being able to measure the γ pair production via pure QCD processes is a necessary step in discriminating between background processes and real Higgs events.

Another important application is the tagging of jets or hadrons with photons in heavy-ion collisions, first suggested in [11]. While photons remain unaffected at LO while traversing the QGP [12], this is not true of strongly-interacting partons, which lose energy via interactions with the soft components of the medium [13, 14], giving rise to so-called “jet-quenching”. One of the most frequently cited experimental observables to confirm the existence of the QGP is given by R_{AA} , defined as the overall factor by which a particular observable was suppressed in nuclear collisions with respect to scaled pp collisions. Unfortunately, as discussed

in Section 4.4, this observable cannot discriminate to a large degree between a wide variety of models for jet quenching. For this reason, it has been suggested that we instead observe the suppression of *photon-tagged* jets and hadrons. Such an observable is much more sensitive to the initial jet energy profile, and so can say more about energy loss in the medium as a function of the path length of the outgoing jet. And just as single γ production in nuclear collisions requires good control of the pp case, an understanding of γ -jet pair suppression necessitates a good control over the baseline prediction for these pairs in pp collisions.

For all of these reasons, both single-particle and two-particle spectra involving photons in hadronic collisions are of essential importance, and it is the goal of this thesis to compute these observables with the highest level of precision possible and compare them, when possible, to existing experimental data.

1.4 Next-to-leading Order Computations

While it is often sufficient to calculate leading-order (LO) cross-sections, it has become very clear in recent years that certain processes have substantial corrections from next-to-leading order (NLO) and sometimes even higher-order processes. This phenomenon is often encoded in a so-called “ K -factor”, which is defined as the ratio of the NLO to LO calculations for a given cross-section computation. For instance, in the case of inclusive jet production, when one chooses typical scales for the computation, a K -factor of 2.8 is prescribed [15] – the NLO corrections are more important than the LO contribution itself! Fortunately, in many cases, K is often constant over a wide p_T range, so that it is legitimate to merely weigh the entire LO calculation with this single factor.

However, for more complicated observables, such as di-particle correlations, this method becomes ineffective. There is new physics that manifests at NLO that no value of K can describe. For instance, in the case of a di-jet cross-section, $2 \rightarrow 2$ kinematic constraints give that $\mathbf{p}_T^{j1} = -\mathbf{p}_T^{j2}$, so that the azimuthal angle between jets must be $\Delta\phi = \pi$. In experiment, we observe a more spread-out distribution, centered around π , but with non-zero contributions spanning the entire azimuth. This is due almost entirely to NLO final-state emission of an extra parton, which allows both the magnitude and the direction of the jet momenta to differ.

In this thesis, we will develop the formalism for both LO and NLO computations, and, in particular, will see that several types of complications arise at NLO:

- $2 \rightarrow 3$ phase space involves more complex kinematic relations, as touched on above.
- NLO matrix elements contain divergences, and so must be computed in d dimensions, with the idea of applying dimensional regularization and ultra-violet (UV) renormalization.
- $2 \rightarrow 2$ diagrams containing a virtual gluon must be taken into account, so as to eliminate the infrared (IR) divergences in the real diagrams.
- In the examined case of hard γ production, there is no longer a concrete distinction between “direct” and “fragmentation” photons, so that more complicated scale dependences arise.
- We will need to come up with new observables (see, for example, Section 4.3.1) to illuminate the relevant higher-order effects that come about.

Overall, the results presented in Chapters 3 and 4 will show the significant increase in accuracy achieved when going to higher order in α_s , and the interesting physical problems it allows us to examine which would not be accessible at LO.

1.5 Outline of Thesis

The thesis will be outlined as follows: In Chapter 2, we will briefly discuss the theoretical ideas underpinning pQCD, including the central notions of asymptotic freedom and confinement. A discussion of higher-order divergences will lead to a presentation of the factorization theorem. For the sake of completeness, we will then discuss the kinematical aspect of such calculations, which will allow us to reach our final goal of calculating full hadronic cross-sections at LO and NLO.

In Chapter 3, we will use our new theoretical tools to actually compute the LO and NLO cross-sections for production of hard photons and pions in $p + p$ collisions at RHIC and LHC energies. Here, we will take a more in-depth look

at how these cross-sections depend on the extra “scales” that come out of the factorization assumption, and we will compare our results to experimental data from the PHENIX and CMS experiments. Since some of the data is obtained using experimental isolation criteria, we will devote a section to describing the theoretical modifications necessitated due to isolation, and compare results obtained with and without these modifications.

Finally, in Chapter 4, we will come to the meat of the thesis, in discussing photon-hadron correlation cross-sections in $p + p$ collisions. As in the preceding chapter, we will compare the LO and NLO computations, and will motivate the need to construct new observables to take into account higher-order effects. The effects of applying isolation criteria to one or both outgoing legs will be considered as well. The chapter will conclude with a qualitative discussion of the usefulness of photon-hadron correlations in nucleus-nucleus collisions, and, in particular, their use in developing a spatial “tomography” of jet energy loss throughout the nuclear medium. This will finally be followed by an overall summary in Chapter 5.

Chapter 2

Perturbative QCD

2.1 Introduction

This chapter will be concerned with an exposition of the fundamental tools needed to compute leading order (LO) and next-to-leading order (NLO) cross-sections for both single-particle and multi-particle spectra. After reviewing basic elements of the scattering-matrix formalism and fundamentals of perturbative QCD (pQCD), we will discuss the running of the strong coupling α_s , including asymptotic freedom and color confinement. Following this, we'll introduce the factorization theorem, and conclude the chapter by discussing LO and NLO kinematics at colliders, setting the stage for a full cross-section computation.

Theoretical discussions more specific to the research content of the thesis are left for the following chapters, including discussions of the modification of energy scales (Subsection 3.2.2), computing isolated cross-sections (Section 3.4), and defining observables for two-particle spectra (Section 4.3.1).

In the interest of maintaining brevity, we relegate discussions of field theory fundamentals to a very short background summary in Appendix A. For a more extensive discussion of the basics of QFT and Feynman diagrams, the reader is referred to [16] or [17]. For more application-oriented reviews of pQCD, [18], [19], and [20] are excellent resources. A more contemporary review article centered around LHC phenomenology is given by [21].

2.2 Cross-sections

Before we start computing pQCD amplitudes in the next section, we want to begin to think about how we'll be relating these to actual physical observables. In fact, most of the theoretical difficulties in QCD have to do with this seemingly “simple” problem of relating theoretically well-defined quantities to experimentally observed ones! It is a problem we will come back to again and again.

In this section, we won't bridge this gap entirely, but we'll come a long way by introducing the scattering-matrix (“S-Matrix”) formalism for *partonic variables*. Our discussion will closely follow the methodology found in several field theory textbooks such as [16, 17].

If we consider two beams of particles of types P and Q that have respective densities ρ_P and ρ_Q , lengths l_P and l_Q , and cross-sectional area A , then we can provide a general definition for the *cross-section* of an interaction. Given n scattering events, we define:

$$\sigma = \frac{n}{\rho_P \rho_Q l_P l_Q A} \quad (2.1)$$

In the case of two beams of constant density, the number of available particles in each beam is given by $N_i = \rho_i l_i A$, and we can rewrite (2.1) as:

$$\sigma = \frac{nA}{N_P N_Q} \quad (2.2)$$

We can think of the cross-section as a method of separating the information about the nature of particle interactions themselves – which should be the same regardless of the experimental setup – with the information about the beam, particle density, and other properties of the apparatus being used. For our purposes, it is also useful to define the notion of the *differential* cross-section, $\frac{d^3\sigma}{d^3p_i}$ which represents the infinitesimal cross-section for observing particle i with momentum p_i . Integrating this quantity over a certain region in momentum space will return the total cross-section for this region, which, in conjunction with (2.1), provides information about the total number of observed final-state particles within a certain momentum range in a collision.

If we consider the collision of a single particle A with a beam of particles B whose cross-sectional density is constant and given by n_B , and in which each

particle approaches A at impact parameter \mathbf{b} , then we have that the number of scattering events is given by:

$$n = n_B \int d^2b \mathcal{P}(\mathbf{b}) \quad (2.3)$$

where $\mathcal{P}(\mathbf{b})$ is the probability of interaction as a function of impact parameter. Substituting (2.3) into (2.2) and setting $N_A = 1$, we obtain:

$$\sigma = \int d^2b \mathcal{P}(\mathbf{b}) \quad (2.4)$$

To obtain the form of $\mathcal{P}(\mathbf{b})$, we can consider two general initial wavepackets ϕ_A and ϕ_B , and N final-state wavepackets given by ϕ_i , $i = 1 \dots N$, The squared scattering amplitude is given by:

$$P = |\langle \phi_1 \phi_2 \dots \phi_N | \phi_A \phi_B \rangle|^2 \quad (2.5)$$

We note a couple of things: a) We are operating in the Heisenberg picture, in which the operators rather than the states evolve in time; b) In this expression, we take each ϕ_i to be spatially localized, since otherwise the wavepackets would have non-zero correlations with one another. If we take the final state to be in the distant future with the respect to the interaction timescale, and the initial state to be in the distant past, then we can express our states as superpositions of momentum eigenstates:

$$\langle \phi_1 \dots \phi_N | = \left(\prod_f \int \frac{d^3 p_f}{(2\pi)^3} \frac{\phi_f(\mathbf{p}_f)}{\sqrt{2E_f}} \right) \langle \mathbf{p}_1 \dots \mathbf{p}_N | \quad (2.6)$$

$$| \phi_A \phi_B \rangle = \left(\prod_{i=A,B} \int \frac{d^3 p_i}{(2\pi)^3} \frac{\phi_i(\mathbf{p}_i)}{\sqrt{2E_i}} \right) e^{-i\mathbf{b} \cdot \mathbf{p}_B} | \mathbf{p}_A \mathbf{p}_B \rangle \quad (2.7)$$

Note that we've made the spatial translation \mathbf{b} between A and B explicit in (2.7). We see that the problem is reduced to computing the correlation amplitudes of these idealized momentum eigenstates, where a large amount of time has elapsed in between initial and final states:

$$\begin{aligned} \lim_{T \rightarrow \infty} \cdot_{(T)} \langle \mathbf{p}_1 \dots \mathbf{p}_N | \mathbf{p}_A \mathbf{p}_B \rangle_{(-T)} &= \langle \mathbf{p}_1 \dots \mathbf{p}_N | \lim_{T \rightarrow \infty} e^{-i2\hat{H}T} | \mathbf{p}_A \mathbf{p}_B \rangle \\ &\equiv \langle \mathbf{p}_1 \dots \mathbf{p}_N | \hat{S} | \mathbf{p}_A \mathbf{p}_B \rangle \quad (2.8) \end{aligned}$$

We can further separate out the interacting portion of our ‘‘S-matrix’’ operator \hat{S} by defining a ‘‘T-matrix’’ such that $\hat{S} \equiv \mathbf{1} + i\hat{T}$. Knowing that \hat{S} (and therefore \hat{T}) must express conservation of 4-momentum, we can rewrite \hat{T} ’s action on the states as:

$$\langle \mathbf{p}_1 \dots \mathbf{p}_N | \hat{T} | \mathbf{p}_A \mathbf{p}_B \rangle = (2\pi)^4 \delta^{(4)}(p_A + p_B - p_1 - \dots - p_N) \mathcal{M}(p_A, p_B \rightarrow p_1, \dots, p_N) \quad (2.9)$$

Accordingly, we have reduced the problem to computing the quantity \mathcal{M} , which for a given process depends only the dynamics described by the interaction Hamiltonian. Returning to Equation (2.4), and considering the case in which all of our final-state particles are momentum eigenstates contained within the region of phase space $d^3 p_1 \dots d^3 p_n$, we can write:

$$\mathcal{P}(\mathbf{b}) = \left(\prod_f \frac{d^3 p_f}{(2\pi)^3 2E_f} \right) |\langle \mathbf{p}_1 \dots \mathbf{p}_N | \phi_A \phi_B \rangle|^2 \quad (2.10)$$

Substituting our expression (Eq. (2.7)) for $|\phi_A \phi_B\rangle$ into (2.10), and in turn substituting this into (2.4), we finally obtain:

$$d\sigma = \left(\prod_f \frac{d^3 p_f}{(2\pi)^3 2E_f} \right) \int d^2 b \left(\prod_{i=A,B} \int \frac{d^3 p_i d^3 k_i \phi_i(\mathbf{k}_i) \phi_i^*(\mathbf{p}_i)}{(2\pi)^6 \sqrt{4k_{0,i} p_{0,i}}} \right) e^{i\mathbf{b} \cdot (\mathbf{p}_B - \mathbf{k}_B)} \langle \mathbf{p}_f | \mathbf{k}_i \rangle \langle \mathbf{p}_f | \mathbf{p}_i \rangle^* \quad (2.11)$$

It is then simple to perform the integration over \mathbf{b} , substitute in (2.9) to relate our expression to \mathcal{M} , and simplify the kinematics contained in the resulting delta functions. This gives us:

$$d\sigma = \left(\prod_f \frac{d^3 p_f}{(2\pi)^3 2E_f} \right) \int \frac{d^3 p_A d^3 p_B}{(2\pi)^6 4E_A E_B} \frac{|\mathcal{M}|^2}{|v_A - v_B|} |\phi_A|^2 |\phi_B|^2 \times (2\pi)^4 \delta^{(4)}(p_A + p_B - p_1 - \dots - p_f) \quad (2.12)$$

Here, we’ve obtained a dependence on the magnitude of the relative beam velocity $|v_A - v_B|$, which we expect for a frame-dependent quantity. We can further perform the p_A and p_B integrals by exploiting the limited resolution of the experimental detector to take these at their average value. Our final expression is given by:

$$d\sigma = \frac{1}{2E_{CM}^2} \left(\prod_f \int \frac{d^3p_f}{(2\pi)^3} \frac{1}{2E_f} \right) |\overline{\mathcal{M}}|^2 (2\pi)^4 \delta^{(4)}(p_A + p_B - \sum_f p_f) \quad (2.13)$$

This is our fundamental equation for computing a partonic differential cross-section given the simplifying laboratory conditions which we’ve exploited. In Section 2.5, we’ll come a bit further and see how this comes into computing an experimentally observable *hadronic* cross-section. In the meanwhile, though, there are already a few interesting things we can find by considering some basic processes in pQCD.

2.3 pQCD Processes

2.3.1 Leading-order amplitudes

The language used to describe the strong interaction at high energies is perturbative Quantum Chromodynamics (pQCD) [22, 23], which can be described at a phenomenological level by the QCD Feynman diagrams for the relevant particles and their interactions. Before QCD was known to be the fundamental theory of the strong interaction, there was still evidence of a substructure in the nucleons and other observed hadrons. This was described by the Parton Model [24, 25, 26], where the label “parton” was used to denote the unknown constituent particles, and is still commonly used to collectively refer to quarks, antiquarks and gluons.

Although, as we’ll see in Section 2.4, partons themselves are never directly observed, we’ll nevertheless spend this section computing *partonic* amplitudes and cross-sections, and seeing the interesting physical problems that arise at this level. It is only in subsequent sections that we’ll worry about how to relate these “unobservable” amplitudes to actual physical observables.

Fundamental to the parton model is the convention that all quarks and gluons are taken to be pointlike and massless, so that the relation $E_i = |\mathbf{p}_i|$ always holds for each component i . This is analogous to considering the frame in which the incoming hadrons have infinite momentum, which is a reasonable assumption to make at high energies.

At LO in QCD, the simplest processes we can consider are $2 \rightarrow 2$ tree-level

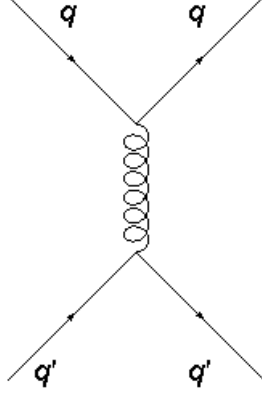


Figure 2.1: The only tree-level Feynman diagram contributing to the process $q + q' \rightarrow q + q'$. Here, and in ensuing diagrams, the time direction extends from left to right.

processes, which are relatively well-behaved. For example, if we consider the tree-level contribution to the process $q(p_1) + q'(p_2) \rightarrow q(p_3) + q'(p_4)$, where q and q' represent two distinct flavors of quark, then there is only a single contributing diagram, given in Figure 2.1. Using the Feynman rules of Appendix A, we can write the corresponding amplitude as:

$$\mathcal{M} = \bar{u}(p_3; s_3, j)(-ig\gamma^\mu(t^a)_i^j)u(p_1; s_1, i)\left(\frac{-i\eta_{\mu\nu}}{k^2}\right)\bar{u}(p_4; s_4, l)(-ig\gamma^\nu(t^a)_k^l)u(p_2; s_2, k) \quad (2.14)$$

Here, $k \equiv p_1 - p_3$, and we've explicitly written out the fermion wavefunctions as a function of their momenta p_i , spins s_i , and flavors i . Taking the amplitude squared and averaging (summing) over initial (final) spin and color, we can simplify this as:

$$\overline{|\mathcal{M}|^2} = \frac{16g^4}{9k^4}((p_3 \cdot p_4)(p_1 \cdot p_2) + (p_3 \cdot p_2)(p_1 \cdot p_4)) \quad (2.15)$$

Substituting this into Equation (2.13), we can simplify the $2 \rightarrow 2$ phase space and write the differential cross-section as:

$$\frac{d\sigma}{d(\cos\theta)} = \frac{2}{9} \frac{\pi\alpha_s^2}{E_{CM}^2} \frac{4 + (1 + \cos\theta)^2}{(1 - \cos\theta)^2} \quad (2.16)$$

In this derivation, we have used the fact that all of the partons are massless, and we have defined θ as the center-of-mass angle between $q(p_1)$ and $q(p_3)$. We can immediately note that, even at LO, this expression is singular: as $\theta \rightarrow 0$, $\frac{d\sigma}{d(\cos\theta)}$

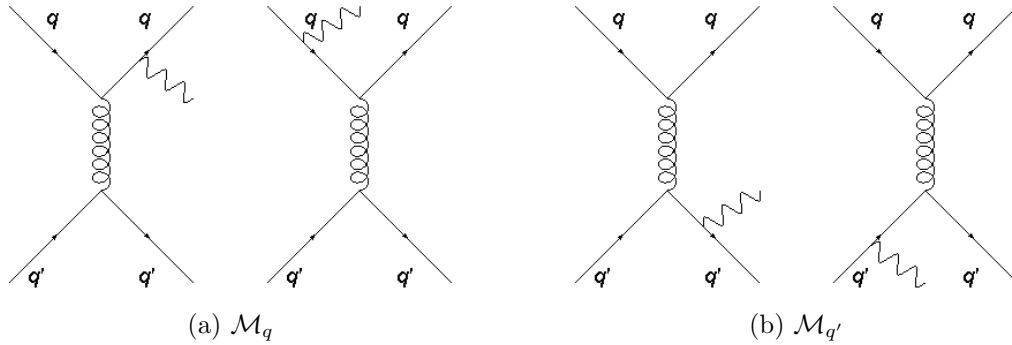


Figure 2.2: Possible tree-level Feynman diagrams for the process $q + q' \rightarrow \gamma + q + q'$, separated into two classes.

diverges. However, we can be comforted by the fact that this result is not unique to QCD – the same singularity will occur in the analogous QED scattering process $e^- + \mu^- \rightarrow e^- + \mu^-$ and arises from the emission of a nearly on-shell photon (or gluon in our case).

2.3.2 Divergences at Next-to-leading order

It is well-known however that at higher orders – either in loop diagrams, or in diagrams with a larger number of final-state particles – more complicated divergences arise in certain regions of phase space. To illustrate this, we can consider the tree-level process $q(p_1) + q'(p_2) \rightarrow q(p_3) + q'(p_4) + \gamma(q)$, which contributes to photon production at NLO. More detailed discussions of this process can be found in [27] and [28].

Considering the case in which q and q' are distinct quark flavors, there are four diagrams that need to be taken into account, given in Figure 2.2. We've separated the diagrams into two in which the radiation is emitted from flavor q and two in which it is emitted from flavor q' . To simplify the calculation, we'll neglect the interference between these two types of diagram (as in [27]; complete treatments of this subprocess, including interference, are given in [28] and [29]), so that $|\overline{\mathcal{M}}|^2 \approx |\overline{\mathcal{M}}_q|^2 + |\overline{\mathcal{M}}_{q'}|^2$. To begin, we can write \mathcal{M}_q as the sum of the two diagrams in 2.2a:

$$\mathcal{M}_q = \frac{iee_q g^2}{(p_4 - p_2)^2} \epsilon_\mu^*(q) [(t_a)_{ij} (t_a)_{kl}] [\bar{u}(p_4) \gamma_\nu u(p_2)] [\bar{u}(p_3) \times \left(\frac{\gamma^\mu (\not{p}_3 + \not{q}) \gamma^\nu}{(p_3 + q)^2} + \frac{\gamma^\nu (\not{p}_1 - \not{q}) \gamma^\mu}{(p_1 - q)^2} \right) u(p_1)] \quad (2.17)$$

For brevity, we've omitted the spin and flavor indices in this expression. As before, we can square this amplitude and use the rules for averaging and summing over states as needed. We obtain:

$$\begin{aligned} |\overline{\mathcal{M}_q}|^2 &= \frac{2}{9} \left(\frac{1}{4} \right) \frac{e^2 e_q^2 g^4}{(p_4 - p_2)^4} \text{Tr}[\not{p}_4 \gamma^\alpha \not{p}_2 \gamma^\beta] \\ &\times \text{Tr} \left[\not{p}_3 \left(\gamma_\alpha \frac{(\not{p}_1 - \not{q})}{(p_1 - q)^2} \gamma^\mu + \gamma^\mu \frac{(\not{p}_3 + \not{q})}{(p_3 + q)^2} \gamma_\alpha \right) \not{p}_1 \left(\gamma_\mu \frac{(\not{p}_1 - \not{q})}{(p_1 - q)^2} \gamma_\beta + \gamma_\beta \frac{(\not{p}_3 + \not{q})}{(p_3 + q)^2} \gamma_\mu \right) \right] \end{aligned} \quad (2.18)$$

We can see by symmetry that the term $\overline{\mathcal{M}_q}^2$ will have the same form as (2.18), with the exchanges $p_1 \leftrightarrow p_2$ and $p_3 \leftrightarrow p_4$. As in the previous section, we can simplify the expression (2.18), substitute it into (2.13), and simplify the $2 \rightarrow 3$ partonic phase space. We choose the frame in which $\mathbf{p}_3 + \mathbf{p}_4 = 0$. We note that, in this case, both the phase space and matrix element should be evaluated in d -dimensions, before applying dimensional regularization to the result.

Before even considering the final expression, we can see immediately that the integrand (2.18) will diverge for the kinematic configurations in which $(p_4 - p_2)^2 = 2E_4 E_2 (1 - \cos \theta_{2,4}) = 0$ and $(p_3 + q)^2 = 2E_3 Q (1 - \cos \theta_{q,3}) = 0$. These correspond respectively to the cases in which $\theta_{2,4} \rightarrow 0$ – the initial-state collinear emission of a gluon from flavor q' – and $\theta_{3,q} \rightarrow 0$ – the final-state collinear emission of the photon from flavor q . The resulting regularized terms are known as *mass/collinear singularities* or *anomalous components* of the cross-section for the process.

Although the explicit result is lengthy, we shall write it in its entirety here, as it will be extremely relevant when we get to our central goal of explaining the factorization theorem. Rather than writing the result in terms of E_i and θ_i , it turns out to be much more useful to describe it in terms of the variables $k \equiv p_2 - p_4$, $x_i = \frac{k^2}{2p_i \cdot q}$, $z = \frac{x_2}{1-x_1}$ and $\tilde{z} = x_1 + x_2$, as in [27]. We have:

$$\begin{aligned}
\frac{d\sigma_q}{d^4q} &= 2 \frac{e_q^2 \alpha_s^2}{\pi k^4} \frac{2}{9} \left(\frac{4\pi e^{-\gamma_E} \mu^2}{Q^2} \right)^\epsilon x_1 x_2 \left(-\frac{1}{\epsilon} \frac{x_1}{1-x_1} [1 + (1-x_1)^2] \frac{1 + (1-z)^2}{z} \right. \\
&- 2 \frac{x_1}{x_2} [2 + (1-x_1)^2 + (1-x_1-x_2)^2 \log \frac{(1-x_1)(x_1+x_2)}{x_2} + \frac{2x_1^2}{(x_1+x_2)^2} - \frac{(x_1+x_2)x_1}{1-x_1} \\
&\left. + 4 \frac{x_1}{x_2} (x_1^2 + x_1 x_2 + x_2^2) - \frac{1}{\epsilon} \frac{x_1 x_2}{x_1+x_2} \frac{(x_1+x_2)^2 + x_1^2}{x_2^2} \frac{1 + (1-\tilde{z})^2}{\tilde{z}} \right) \quad (2.19)
\end{aligned}$$

In this expression, we've defined $Q \equiv (1-\tilde{z})^{\frac{k^2}{x_2}}$, and $\epsilon \equiv 4-d$, so that evaluating the expression in four spacetime dimensions requires taking $\epsilon \rightarrow 0$, and we've had to introduce a new energy scale μ^2 to preserve the correct energy dimensions in d -dimensional spacetime. The expression for $\frac{d\sigma_{q'}}{d^4q}$ will have the same form, with the exchange $x_1 \leftrightarrow x_2$.

The merit in writing the result (2.19) down explicitly will become evident in Section 2.5, where we illustrate how the $\frac{1}{\epsilon}$ divergences are absorbed into the hadronic distribution functions. Although we judiciously chose a process in which we did not need to consider loop corrections, these will in general bring about UV divergences that need to be treated through renormalization, which we discuss in the following section.

2.4 Asymptotic Freedom and Color Confinement

2.4.1 The running of the coupling constants

As with the other field theories that are part of the SM, a renormalization procedure needs to be applied to QCD to deal with the UV divergences that arise in the theory. Initial proofs of renormalizability were given by [30, 31, 32]. In general, renormalizing a field theory results in all the free parameters in the Lagrangian acquiring a dependence on the energy scale of the measurement. In addition, regardless of which procedure is used to regulate and renormalize the theory, a new “renormalization scale” μ with the dimensions of energy needs to be introduced into the theory. In the case of QCD, our parameters are the quark masses m_f and the coupling constant α_s , which we rewrite as $m_f(\mu^2)$ and $\alpha_s(\mu^2)$, respectively.

Since we are dealing with massless QCD, the only constant in our theory that requires renormalization is α_s , which should satisfy the RG equation:[33]

$$\mu^2 \frac{d\alpha_s}{d\mu^2} = \beta(\alpha_s) = -\alpha_s^2(\beta_0 + \beta_1\alpha_s + \beta_2\alpha_s^2 + \dots) \quad (2.20)$$

For the purposes of this thesis, we will only require the first term on the right-hand side for LO calculations, and the first two terms for NLO calculations. In the \overline{MS} renormalization scheme, we can calculate $\beta_0 = \frac{1}{4\pi}(11 - \frac{2}{3}n_f)$ and $\beta_1 = \frac{1}{(4\pi)^2}(102 - \frac{38}{3}n_f)$, obtained from the one-loop and two-loop corrections to the $q\bar{q}g$ vertex respectively [22]. In these expressions, n_f refers to the number of flavors being considered. If we take equation (2.20) at leading-order, we can solve the differential equation with initial conditions $\mu = \mu_0$, $\alpha_s(\mu^2) = \alpha_s(\mu_0^2)$ to get:

$$\alpha_s(\mu^2) = \frac{\alpha_s(\mu_0^2)}{1 + \beta_0\alpha_s(\mu_0) \log\left(\frac{\mu^2}{\mu_0^2}\right)} \quad (2.21)$$

If we define a value $\Lambda_{QCD}^2 = \mu_0^2 e^{-\frac{1}{\beta_0\alpha_s(\mu_0^2)}}$ (known as the *QCD Scale*), and substitute in our value for β_0 , we can reexpress our coupling constant as:

$$\alpha_s(\mu^2) = \frac{12\pi}{(33 - 2n_f) \log\left(\frac{\mu^2}{\Lambda_{QCD}^2}\right)} \quad (2.22)$$

The value of Λ_{QCD} cannot be obtained theoretically, and must, in fact, be extracted from experimental data. The current standard is to evaluate α_s for the value $\mu = M_Z$, where M_Z is the mass of the Z-boson, and then extrapolate to obtain a value for Λ_{QCD} . In practice, we also choose n_f , depending on whether our energy scale exceeds the mass of a given species of quark. The value of Λ for a given n_f is obtained by requiring α_s to be a continuous function of μ as one “crosses” between energy scales. For instance, when crossing the threshold for the production of bottom quarks, we would take $\alpha_s(\mu = m_b, n_f = 5, \Lambda_5) = \alpha_s(\mu = m_b, n_f = 4, \Lambda_4)$. [34]

We can notice immediately that, independent of our unknown scale, we will have α_s going to 0 as $\mu \rightarrow \infty$: this is the property known as *asymptotic freedom*. At large energies, the coupling constant of QCD becomes small enough to enable us to use perturbation theory to describe the interactions of quarks and gluons. It is, on the contrary, at lower energy scales that perturbative QCD fails, and numerical methods such as lattice QCD must be used to be able to make any computations.

At NLO, we must solve the differential equation:

$$\log\left(\frac{\mu^2}{\mu_0^2}\right) = - \int_{\alpha_s(\mu_0)}^{\alpha_s(\mu)} \frac{d\alpha}{\alpha^2(\beta_0 + \beta_1\alpha)} \quad (2.23)$$

which is done by performing an elementary integration of the right-hand side, resulting in:

$$\log\left(\frac{\mu^2}{\mu_0^2}\right) = \frac{\beta_1}{\beta_0^2} \log \alpha_s + \frac{1}{\beta_0 \alpha_s} - \frac{\beta_1}{\beta_0^2} \log\left(\alpha_s + \frac{\beta_0}{\beta_1}\right) + c \quad (2.24)$$

By once again defining an appropriate Λ that can absorb the integration constant c containing information about some reference scale $(\mu_0, \alpha_s(\mu_0^2))$, we obtain a final two-loop implicit expression for our coupling:

$$\log\left(\frac{\mu^2}{\Lambda^2}\right) = \frac{1}{\beta_0 \alpha_s} - \frac{\beta_1}{\beta_0^2} \log\left(\frac{\beta_1}{\beta_0^2} + \frac{1}{\beta_0 \alpha_s}\right) \quad (2.25)$$

Obviously, it requires numerical or iterative techniques to make this implicit expression explicit. We will note that, when we do actual computations in subsequent chapters, the JETPHOX [35, 36] and DIPHOX [10] programs used to compute cross-sections are able to internally evaluate the strong coupling at both LO and NLO. In single particle spectra, we will generally take the renormalization scale μ to be the transverse momentum p_T of the outgoing particle, although we will do a brief examination of how an alteration of this scale affects the calculation in Chapter 3. In Figure 2.3, we plot $\alpha_s(\mu)$ (where a numerical method [33] has been used to approximate the NLO expression (2.25)) for the energy regime explored in later calculations, and note that there can be a significant difference between the LO and NLO results.

We finally note that, in the case of QED, for LO computations we will take the coupling α to be a constant of order $\sim 1/137$, and in the NLO case, we calculate it to one-loop, using the same renormalization prescription as above. As before, in the massless limit only the running of the coupling $\alpha(\mu)$ is relevant, and is obtained by solving (2.20) at leading-order with $\beta_0 = -2/3\pi$. [16]

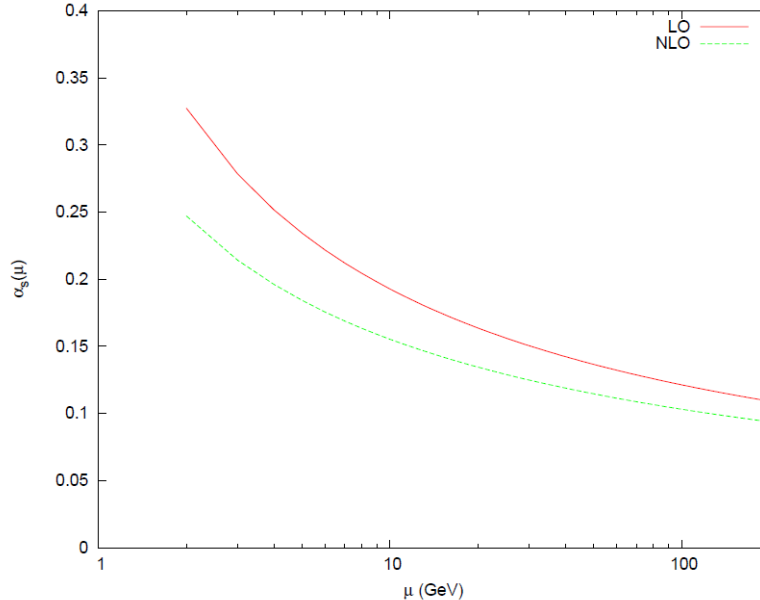


Figure 2.3: α_s plotted at LO and NLO as a function of the energy scale μ . The NLO curve is an approximate solution to Equation (2.25).

2.4.2 Color Confinement

The running of the strong coupling does not only imply asymptotic freedom for high energies – the fact that our coupling becomes non-perturbative at low energy implies that the force between two colored objects would in theory diverge as they were separated to an arbitrarily large distance. Fortunately, we do not observe this property in, for example, atomic nuclei, which are fundamentally composed of color-charged quarks and gluons. Why not? It turns out that protons, neutrons, and all other currently observed baryons and mesons are composed of combinations of quarks whose sum is color neutral. This is the property of *color confinement*, which can be heuristically depicted as in Figure 2.4, borrowed from [37].

In QCD as in other quantum field theories, the vacuum is a dynamic entity, constantly creating and annihilating virtual particles on a time-scale permissible by the Heisenberg uncertainty principle $t \sim \hbar/E$. As a force is applied to separate the quark and anti-quark from one another, the gluon-mediated force between them increases as a result of the increase in α_s at larger distances. At a certain threshold distance, there is actually enough energy in the system so that it is energetically possible to create a new *real* $q - \bar{q}$ pair. Instead of splitting the meson

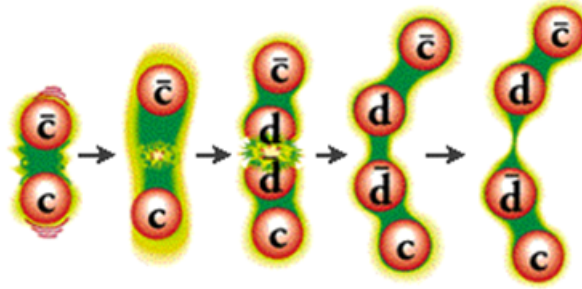


Figure 2.4: A heuristic illustration of color confinement. As the meson is pulled apart, enough energy is added to the system to create a new real quark-antiquark pair. The cartoon is borrowed from [37].

in two, we have only succeeded in creating a new one. Although this explanation is purely qualitative, it serves as the intuitive basis for understanding the processes of fragmentation and hadronization, which we now examine in a more quantitative framework.

2.5 The Factorization Theorem

2.5.1 Introduction

At first glance, we might consider ourselves lucky that the current available collider energies fall well into the perturbative regime, so that we can get away with using the pQCD formalism as described in the preceding sections, and not worry much about low-energy divergences. While it is true that, as per Figure 2.3, α_s is much less than 1 at RHIC and LHC energies, the phenomenon of color confinement prohibits us from actually “seeing” the final-state quarks and gluons in our detectors, despite the fact that these are the entities we are actually dealing with in our Feynman diagrams. Accordingly, we need a formal way of relating the partonic variables to our experimental observables, which are in fact confined hadronic states. This problem is de facto non-perturbative, and is solved by implementing what is known as the *factorization theorem* [38, 39].

Considering a collision between two hadrons A and B , and the corresponding production of hadrons h_1 and h_2 , we have two similar problems to solve: 1. How do we mathematically describe the distributions of our initial partons within the col-

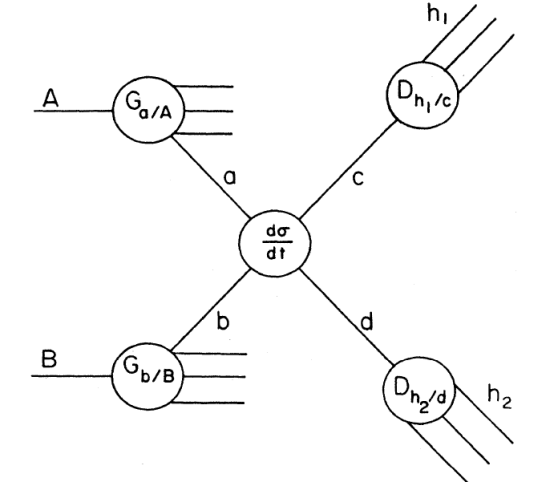


Figure 2.5: A schematic of the collision of two hadrons A and B , the ensuing partonic interaction $ab \rightarrow cd$, and final-state fragmentation of jets into observed hadrons. The diagram is borrowed from [40].

liding hadrons? and 2. How do we relate the phase space distribution of observed final-state hadrons to final-state partons? These issues are treated by the respective introduction of initial-state *Parton Distribution Functions* (PDFs) and final-state *Fragmentation Functions* (FFs) that contain the relevant non-perturbative information. We define our PDF $G_{i/I}(x_i)$ as the probability distribution for finding parton i with momentum fraction x_i in hadron I . We similarly define our FF $D_{h/j}(z_h)$ as the distribution for obtaining hadron h with momentum fraction z_h from parton j . At the most basic level, we expect that convolving the partonic cross-section with the PDFs for both incoming partons and the FFs for the outgoing ones should give us a total cross-section for the process $A + B \rightarrow h_1 + h_2$. We give a schematic for this idea in Figure 2.5, borrowed from [40].

In fact, this cannot be exactly true, since the partonic physics and hadronic physics must be interrelated – it is necessary for us to introduce an unphysical scale Q in the initial-state (and a second scale Q_F in the final-state) at which to separate the small-distance and large-distance effects. More quantitatively, Q (Q_F) is a scale at which we begin to factor out our initial-state (final-state) collinear divergences at all orders in perturbation theory, and absorb them into the non-perturbative distributions.

In the following subsection, we will consider in a more rigorous manner the

relevant case of initial-state and final-state factorization in high- p_T γ production. This will in fact form the basis of our theoretical computations in Chapter 3.

2.5.2 Factorization in photon production

As in the case of hadronic production, there is a probability distribution for an outgoing parton to fragment into a photon with momentum fraction z , denoted by $D_{\gamma/c}(z)$. If we consider the process $p + p \rightarrow \gamma + X$ at fixed-order in α_s , where X represents any other particles produced in the process, then we can mathematically express the factorization theorem for this process as follows :

$$d\sigma^{(F)}(p + p \rightarrow \gamma + X) = \sum_{a,b,c,d} G_{a/p}(x_a) dx_a G_{b/p}(x_b) dx_b D_{\gamma/c}(z_c) dz_c d\hat{\sigma}(a + b \rightarrow c + d) \quad (2.26)$$

Here, $G_{i/p}(x_i)$ and $D_{\gamma/c}(z_c)$ are respectively PDFs and FFs defined as in the previous subsection, and $\hat{\sigma}$ is a partonic cross-section for process $ab \rightarrow cd$. At the most basic conceptual level, the equation states that the probability of observing a hard photon in a $p + p$ collision is the probability that a parton c is produced via any permitted Feynman diagram, weighted by the PDFs for each initial parton and by the FF for obtaining a γ in the fragmentation jet of c . The (F) superscript denotes the fact that this is a “fragmentation photon”.

Although the FFs are in general non-perturbative, because of the pointlike coupling of the quark and γ it is actually possible to perturbatively derive the LO expression for $D_{\gamma/q}(z)$ [27], which is given by:

$$D_{\gamma/q}^{(0)}(z) = \frac{\alpha}{2\pi} e_q^2 \left(\frac{1 + (1 - z)^2}{z} \right) \log \left(\frac{Q^2}{\Lambda^2} \right) \quad (2.27)$$

Because there is no gluon-photon vertex, $D_{\gamma/g}^{(0)}(z) = 0$. As we expect from our earlier argument, these expressions contain a dependence on a new energy parameter Q . We will discuss the higher-order non-perturbative corrections to these in Subsection 2.5.4.

We can also note that, unlike in the case of hadrons, there is also a “direct” method of photon production, due to the $q\bar{q}\gamma$ vertex in QED. This cross-section can be expressed as:

$$d\sigma^{(D)}(p+p \rightarrow \gamma+X) = \sum_{a,b,d} G_{a/p}(x_a)dx_a G_{b/p}(x_b)dx_b d\hat{\sigma}(a+b \rightarrow \gamma+d) \quad (2.28)$$

While the LO contribution of (2.28) will be finite, higher-order corrections will suffer from ultraviolet (UV), infrared (IR), and collinear divergences, as illustrated in Section 2.3. The UV divergences are taken care of with the renormalization procedure, and, for sufficiently inclusive processes, the IR divergences are cancelled exactly when summing the virtual correction diagrams of a given order with the higher-order real production diagrams. The factorization theorem comes in when we attempt to deal with collinear divergences. In this case, it states that, at a given order in α_s , the sum of (2.26) and (2.28) will be infrared safe – the divergences arising from the “direct” production of two collinear partons can always be absorbed into the non-perturbative “fragmentation” contribution. For instance, at $\mathcal{O}(\alpha_s)$, this gives us:

$$d\sigma^{(1)} = d\sigma_{(D)}^{(1)}(ab \rightarrow \gamma d) + \sum_c d\sigma_{(F)}^{(0)}(ab \rightarrow cd) \otimes D_{\gamma/c}^{(1)} \quad (2.29)$$

The factorization theorem implies that this quantity will be finite. To provide a specific illustration of this, we can go back to our final expression (2.19) for the process $qq \rightarrow qq\gamma$. If we look at the final term, which was divergent due to a $\frac{1}{\epsilon}$ dependence, we can show that this term in fact corresponds precisely to our cross-section (2.16) for $qq \rightarrow qq$ (reexpressed in terms of the variables x_1 and x_2), multiplied by the LO FF given in (2.27). This means that *part of the anomalous direct cross-section can be exactly absorbed into the fragmentation cross-section of a given order!*

To explain the other anomalous term (the first term in (2.19)), we invite the reader to check that this corresponds precisely to the LO result for the process $qq \rightarrow \gamma q$, multiplied by the anomalous probability function $P_{qg}(z)$ (known commonly as an Altarelli-Parisi splitting function [41]) for the initial-state quark to emit a collinear gluon.

In this way, these two terms are no longer taken to form part of the “direct” cross-section for $qq \rightarrow qq\gamma$, but are now subtracted and taken as respective corrections to the LO final-state and initial-state distribution functions. We heuristically illustrate this result in Figure 2.6.

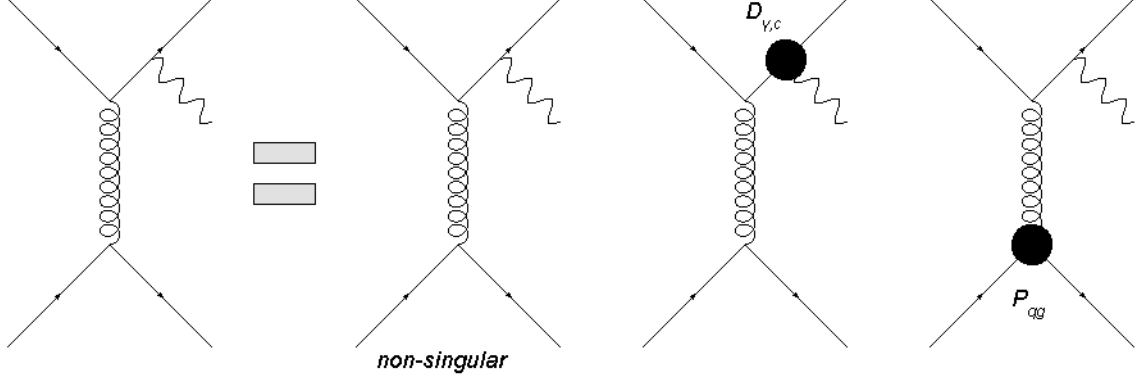


Figure 2.6: A heuristic depiction of how the singularities in $qq \rightarrow qq\gamma$ are factorized and absorbed into the relevant initial-state and final-state distribution functions.

2.5.3 Fitting PDFs and FFs

Because the PDFs and FFs cannot be calculated perturbatively to arbitrary order, they must be determined from experimental data fits to various processes (Deep Inelastic Scattering (DIS), di-lepton production, jet production, etc.) at a given energy scale. Traditionally, DIS processes (i.e.: $e^- + p \rightarrow e^- + X$) in which a virtual photon probes the internal structure of the proton, were considered to be ideal for resolving the distribution functions. However, it was found that the DIS data did not offer sufficient sensitivity to the gluon PDF, which led to the need for *global* data fits that exploited data from multiple complementary processes.

With respect to the PDFs, several different parameterizations from different groups [42, 43, 44] are in common usage, so, in the following chapters, we will always specify the dataset being used. In general, the convention in fitting a given PDF is to assume a set of functional forms like [43]:

$$\begin{aligned}
 xq_v(x) &= A_u x^{\eta_1} (1-x)^{\eta_2} (1 + \epsilon_u \sqrt{x} + \gamma_u x) \\
 xd_v(x) &= A_d x^{\eta_3} (1-x)^{\eta_4} (1 + \epsilon_d \sqrt{x} + \gamma_d x) \\
 xS(x) &= A_S x^{\delta_S} (1-x)^{\eta_S} (1 + \epsilon_S \sqrt{x} + \gamma_S x) \\
 x\Delta(x) &= A_\Delta x^{\eta_\Delta} (1-x)^{\eta_S+2} (1 + \gamma_\Delta x + \delta_\Delta x^2) \\
 xg(x) &= A_g x^{\delta_g} (1-x)^{\eta_g} (1 + \epsilon_g \sqrt{x} + \gamma_g x) + A_{g'} x^{\delta_{g'}} (1-x)^{\eta_{g'}}
 \end{aligned} \tag{2.30}$$

In (2.30), $q_v \equiv q - \bar{q}$ is the *valence quark* distribution, $S \equiv 2(\bar{u} + \bar{d}) + s + \bar{s}$ is the *sea quark* distribution, and $\Delta \equiv \bar{d} - \bar{u}$. We have omitted an additional pair

of equations parameterizing the strange and anti-strange distributions, as well as those of the heavier quarks, which are generally neglected at lower energies. Including the s and \bar{s} distributions, there are 34 parameters to be fit. In the case of the proton, composed of valence quarks uud , four of these are eliminated by invoking the number sum and momentum sum rules [45]:

$$\begin{aligned}
N_u = \int_0^1 dx u_v(x) = 2 & & N_d = \int_0^1 dx d_v(x) = 1 & & N_s = \int_0^1 dx s_v(x) = 0 \\
& & \int_0^1 dx x(u + \bar{u} + d + \bar{d} + s + \bar{s}) = 1 & &
\end{aligned}
\tag{2.31}$$

This leaves a total of 30 parameters to be fit using experimental data. The numerical values of the parameters for the MRST group can be obtained in [43]. In general, these parameters are calculated at a reference scale of $Q_0^2 = 1\text{GeV}^2$. However, as we've established, the PDFs cannot possibly be fixed scale-independent distributions, since they depend on an unphysical chosen scale Q that separates the ‘‘hadronic physics’’ from the ‘‘partonic physics’’. We will explore this scale dependence in the following subsection.

For the sake of brevity, we won't go through the parameterization schemes for the FFs for hadrons and photons, although it suffices to say that these fitting procedures are very similar to the one described above for the PDFs : 1. Functional forms for the distributions are assumed, with a fixed number of unknown parameters; 2. Certain symmetry arguments can be employed to reduce the number of parameters; and 3. The remaining parameters are ‘‘globally’’ fit using experimental data from multiple processes. For fragmenting hadrons, the current standard is to employ the BKK [46] or newer KKP [47] FFs, and for photons there are two parameterizations both described in [48]. Specific information on the functional forms of these distributions can be found contained within these references.

2.5.4 Scale Dependences

As already mentioned, PDFs and FFs necessarily acquire a dependence on a pair of new scaling parameters, respectively called the factorization and fragmentation

scales Q and Q_F . In the case of the PDFs, once the distributions (2.30) are parameterized at scale Q_0^2 , the evolution to an arbitrary scale Q^2 is given by the DGLAP equations [41, 49, 50] for the quark and gluon PDFs:

$$\frac{dG_{q/A}(x, Q)}{d \log Q^2} = \frac{\alpha_s}{2\pi} \int_x^1 \frac{dz}{z} [G_{g/A}(x, Q)P_{qg}(x/z) + G_{q/A}(x, Q)P_{qq}(x/z)] \quad (2.32)$$

$$\frac{dG_{g/A}(x, Q)}{d \log Q^2} = \frac{\alpha_s}{2\pi} \int_x^1 \frac{dz}{z} [G_{g/A}(x, Q)P_{gg}(x/z) + \sum_{q_j} G_{q_j/A}(x, Q)P_{gq_j}(x/z)] \quad (2.33)$$

where P_{ab} are the Altarelli-Parisi splitting functions [41] from parton a to parton b . We can physically interpret these as the perturbatively calculable probability distributions for obtaining parton b from parton a . There is a similar set of equations that can be derived for the scale evolution of the FFs [51, 52]. For instance, in the case of $D_{\gamma/c}(z, Q_F)$, using the shorthand \otimes to describe the convolution integrals as in (2.32) and (2.33), we can write:

$$\frac{dD_{\gamma/q}(Q^2)}{d \log Q^2} = \frac{\alpha}{2\pi} P_{q \rightarrow \gamma} + \frac{\alpha_s(Q^2)}{2\pi} [P_{q \rightarrow g} \otimes D_{\gamma/g}(Q^2) + P_{q \rightarrow q} \otimes D_{\gamma/q}(Q^2)] \quad (2.34)$$

$$\frac{dD_{\gamma/g}(Q^2)}{d \log Q^2} = \frac{\alpha_s(Q^2)}{2\pi} [P_{g \rightarrow q} \otimes D_{\gamma/q}(Q^2) + P_{g \rightarrow g} \otimes D_{\gamma/g}(Q^2)] \quad (2.35)$$

In particular, we can note the interesting fact that since the γ FFs are proportional to $\frac{\alpha}{\alpha_s(Q^2)}$, and $2 \rightarrow 2$ parton processes go as α_s^2 , the convolution of these two should go roughly as $\alpha\alpha_s$. So we have every right to expect that the LO fragmentation γ contribution is in fact of the same order as the direct contribution.

Unfortunately, there is no way of knowing the precise scales Q , Q_F (or the renormalization scale μ) to choose in a given calculation, since they are unphysical scales that are really artifacts of cutting off the perturbative expansion. Fortunately, a quick trick [40] shows us that all scales must be at least of the same order of magnitude. Supposing that we have *two* large scales Q_1^2 and $Q_2^2 = kQ_1^2$, we can note that:

$$\log Q_2^2 = \log(kQ_1^2) = \log Q_1^2(1 + \frac{\log k}{\log Q_1^2}) \approx \log Q_1^2 \quad (2.36)$$

where we’ve used the fact that Q_1 is a “large” scale to drop the second term in parentheses, which is logarithmically nonleading. Even following this argument, we are still forced to decide how we want to define our single large energy scale : we are obliged to select a *factorization prescription*. Although this is by no means an obvious procedure, and various methods to do this have been proposed [53, 54], we will adopt the convention most in use currently: 1. PDFs and FFs are experimentally defined using some reference processes (as in Subsec. 2.5.3); and 2. The factorization scales are taken to be a *function of the kinematic variables* of the process being examined.

Most often we will select the scales such that $\mu = Q = Q_F = p_T$, where p_T is the transverse momentum of the fragmenting particle, although in Subsection 3.2.2, we briefly examine the effect of modifying these parameters. The choice of which kinematic variables to use becomes a bit more ambiguous when considering double inclusive processes, in which we are observing two final-state particles with unequal transverse momenta. Possible choices in this case include taking scales to be equal to $p_{T,1} + p_{T,2}$, $\max(p_{T,1}, p_{T,2})$, or $M_{1,2}$ (the invariant mass of particles 1 and 2), though these choices are by no means exhaustive.

For any calculation at a given order, we can consider the result’s variation with respect to these parameters to be a theoretical systematic uncertainty. As one goes to higher order, the dependence on these parameters becomes less important, which offers another important benefit of going to NLO.

As a final note, we mention that, in sections to follow, we will often not explicitly write out the Q or Q_F dependences of the PDFs or FFs respectively, but remind the reader that they are always there.

2.6 Hadronic Kinematics

2.6.1 Leading order

Keeping track of the kinematic relationships in a hadronic cross-section calculation is necessary to determine both the range of integration as well as the appropriate Jacobian that arises through simplification of delta functions. This is slightly more complicated than in the partonic case, since we now operate in the hadronic CM

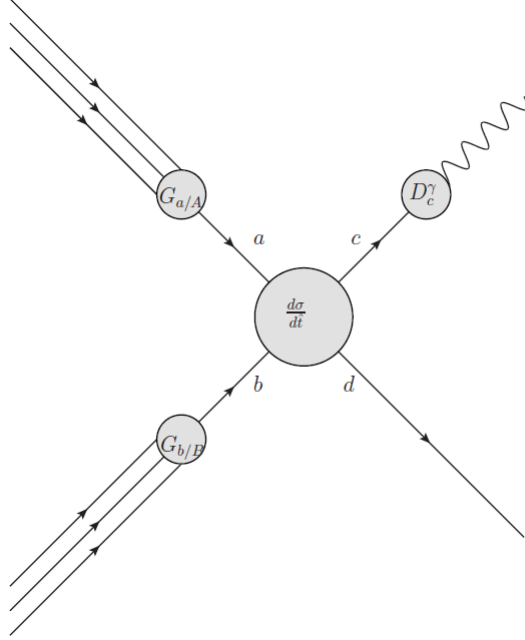


Figure 2.7: A schematic of the collision of two hadrons A and B , the ensuing partonic interaction $ab \rightarrow cd$, and final-state production of a fragmentation photon γ and a jet d .

frame rather than the partonic one. To conclude this chapter, we will briefly work through an example of this type of manipulation here, in which we consider the calculation of the leading-order double inclusive cross-section of a fragmentation photon with an away-side jet in the collision of two hadrons A and B . Note that this result would also describe, for example, the double inclusive cross-section of an away-side direct photon with a fragmenting hadron, when the appropriate substitutions are made. A schematic diagram of this type of process is shown in Figure 2.7.

Defining the partonic four-momenta as p_a , p_b , p_c , and p_d , and combining equations (2.26) and (2.13), we can write down the expression for the differential cross-section for this process:

$$\begin{aligned}
 d\sigma(AB \rightarrow cd) = \sum_{abcd} G_{a/A}(x_a) dx_a G_{b/B}(x_b) dx_b D_{\gamma/c}(z) dz \frac{|\overline{\mathcal{M}}|^2}{2E_{CM}^2} \\
 \times (2\pi)^4 \delta^{(4)}(p_a + p_b - p_c - p_d) \frac{d^3 p_c}{(2\pi)^3 2E_c} \frac{d^3 p_d}{(2\pi)^3 2E_d} \quad (2.37)
 \end{aligned}$$

Here, $|\overline{\mathcal{M}}|^2$ is the matrix element for a given subprocess, averaged over initial-state color and spin, and the PDFs and FFs are as defined previously. We also define \sqrt{s} as the hadronic center-of-mass (CM) energy, and we introduce the variable $y_i \equiv \log(\cot \theta_i/2)$, referred to as the *pseudorapidity* of parton i . From here on out, we will need to choose a frame to work in, and the one that makes the most sense is the hadronic CM frame, since this is identical to the lab frame for colliders like RHIC or LHC. In this case, we can write down explicit expressions for all of the p_i in terms of external hadronic variables:

$$\begin{aligned}
p_a &= \frac{x_a \sqrt{s}}{2} (1, 0, 0, 1) \\
p_b &= \frac{x_b \sqrt{s}}{2} (1, 0, 0, -1) \\
p_c &= (p_T^c \cosh y_c, \mathbf{p}_T^c, p_T^c \sinh y_c) \\
p_d &= (p_T^d \cosh y_d, \mathbf{p}_T^d, p_T^d \sinh y_d)
\end{aligned} \tag{2.38}$$

It is also convenient to define an additional set of variables – the partonic *Mandelstam variables* – which are defined as:

$$\begin{aligned}
\hat{s} &= (p_a + p_b)^2 = x_a x_b s \\
\hat{t} &= (p_a - p_c)^2 = -x_a p_T \sqrt{s} e^{-y_c} \\
\hat{u} &= (p_b - p_c)^2 = -x_b p_T \sqrt{s} e^{y_c}
\end{aligned} \tag{2.39}$$

For instance, Equation (2.15), which would describe a relevant subprocess in this example, would be more conventionally written as $|\overline{\mathcal{M}}|^2 = 16\pi^2 \alpha_s^2 \frac{4}{9} \frac{\hat{s}^2 + \hat{u}^2}{\hat{t}^2}$. After writing all squared matrix elements in terms of the variables \hat{s} , \hat{t} , and \hat{u} , the relations (2.39) can be used to express them in terms of the integration variables. We are now prepared to simplify equation (2.37), by noting:

- $\frac{d^3 p_i}{E_i} = \frac{d^2 p_T^i d p_z^i}{E} = d^2 p_T^i dy_i$.
- $\delta^{(4)}(p_a + p_b - p_c - p_d) = \delta\left(\frac{x_a \sqrt{s}}{2} + \frac{x_b \sqrt{s}}{2} - p_T^c \cosh y_c - p_T^d \cosh y_d\right) \times \delta\left(\frac{x_a \sqrt{s}}{2} - \frac{x_b \sqrt{s}}{2} - p_T^c \sinh y_c - p_T^d \sinh y_d\right) \times \delta^{(2)}(\mathbf{p}_T^c + \mathbf{p}_T^d)$
- $\frac{d\sigma}{d\hat{t}} = \frac{1}{16\pi \hat{s}^2} |\overline{\mathcal{M}}|^2$

Before substituting all of this in, we note that the four δ -functions will be able to eliminate four integration variables in our expression. Naturally, since we are

looking for the *double inclusive* cross-section for a jet and a fragmentation photon, we would like to have our differential cross-section as a function of $y_\gamma = y_c, y_d, \mathbf{p}_T^d$, and z . Accordingly, we choose to eliminate x_a, x_b , and \mathbf{p}_T^c , which will give us our “kinematic constraints” for the problem. Putting this all together, we get:

$$d\sigma(A+B \rightarrow \gamma+jet+X) = 2 \sum_{abcd} G_{a/A}(x_a)G_{b/B}(x_b)D_{\gamma/c}(z)\frac{d\sigma}{dt}(ab \rightarrow cd)dzdy_\gamma dy_d p_T^d dp_T^d \quad (2.40)$$

Our constraints are given by $x_{a,b} = \frac{p_T^d}{\sqrt{s}}(e^{\pm y_\gamma} + e^{\pm y_d})$ and $\mathbf{p}_T^d = -\mathbf{p}_T^c = -\mathbf{p}_T^\gamma/z$. The latter of these confirms that, at LO, the two final-state jets must have opposite transverse momenta, as expected. The ranges of integration for the two rapidities will be set by the detector in question, while z will range from some kinematically specified minimum value z_{min} to 1. To obtain the *single* inclusive cross-section for fragmentation γ production, the most natural way would have been to eliminate the variables y_d, \mathbf{p}_T^d , and z , leaving the cross-section as an integral over the x_a and x_b variables, which could then be numerically evaluated.

2.6.2 Next-to-leading order

As a last point for this chapter, let us consider the type of kinematic expressions we would deal with for a higher-order (i.e.: $2 \rightarrow 3$) process, which are necessary to compute when going to higher order in α_s . We expect a priori from our earlier discussion that there will be soft or collinear divergences for the relevant partonic cross-sections, so we must write our expression in $n = 4 - 2\epsilon$ dimensions, with the idea of later applying dimensional regularization to our expression.

Considering the general process $A + B \rightarrow c + d + e$, we have:

$$d\sigma(AB \rightarrow cde) = \sum_{abcde} G_{a/A}(x_a)dx_a G_{b/B}(x_b)dx_b \frac{|\bar{\mathcal{M}}|^2}{2\hat{s}} \times (2\pi)^n \delta^{(n)}(p_a + p_b - p_c - p_d - p_e) \frac{d^n p_c \delta(p_c^2)}{(2\pi)^{n-1}} \frac{d^n p_d \delta(p_d^2)}{(2\pi)^{n-1}} \frac{d^n p_e \delta(p_e^2)}{(2\pi)^{n-1}} \quad (2.41)$$

In general, partons c and d can be considered to be well-separated in phase space, and have a certain minimum p_T , so that they do not introduce any infrared divergences. In this case, parton e can be taken to branch off from either c or d , and

potentially introduce divergences as a result. We can control the divergences by introducing two unphysical parameters p_T^m and R_T^h that separate phase space into four distinct regions. This method is in fact the numerical basis of the programs JETPHOX [35, 36] and DIPHOX [10], used in the following chapters for NLO computations. The four regions are given by:

- $p_T^e < p_T^m$. This region contains the soft and initial-state collinear singularities.
- $p_T^e > p_T^m$ and \mathbf{p}_e is contained in a cone around c given by $\{(y_e - y_c)^2 + (\phi_e - \phi_c)^2 < R_T^2$. This region contains singularities arising from e being collinear to c .
- $p_T^e > p_T^m$ and \mathbf{p}_e is contained in a cone around d given by $\{(y_e - y_d)^2 + (\phi_e - \phi_d)^2 < R_T^2$. This region contains singularities arising from e being collinear to d .
- $p_T^e > p_T^m$ and p_T^e is not contained in either of the two defined cones. This defines the non-singular contribution that does not need to be factorized.

In this way, a well-defined numerical method exists with which to compute NLO cross-sections. Ideally, the routines used within a given program are such that the theoretical dependence on the parameters p_T^m and R_T^h is minimized.

We have now built up all of the tools we need to explicitly calculate single and multi-particle spectra, for which we display our results in Chapter 3 and 4 respectively.

Chapter 3

Photon Production

3.1 Introduction

The observation of electromagnetic signatures in hadronic and heavy-ion collisions is of fundamental importance in probing these media. In the hadronic case, for instance, hard photon production is very sensitive to the initial gluon distributions [8], as a result of the dominance of the QCD Compton process $q + g \rightarrow q + \gamma$ at LO. An analysis of γ production in $p + p$ and $p + \bar{p}$ collisions also offers an important method of computing the strong coupling constant α_s [9]. Additionally, having precise predictions for γ cross-sections is also very important with regards to detection of the Higgs boson: one of the primary Higgs decay channels is via $H \rightarrow \gamma\gamma$ [10], which can only usefully be measured if one has control over the background of γ pairs with large invariant mass.

In the case of nucleus-nucleus collisions, photon-jet or photon-hadron correlations offer insight into the mechanism of jet quenching in the thermal medium by constraining the initial jet energy profiles before energy loss [55, 56]. This will be explored to a greater extent in the final section of Chapter 4. Additionally, in both hadronic and nuclear cases, photon measurements allow one to avoid having to deal with either jet reconstruction algorithms or jet fragmentation functions in the leading-order (LO) case, unlike in computations of jet or hadron cross-sections respectively.

Following the standard convention, in this chapter we use the term “prompt photon” to denote those photons produced in a collision that are not the result of

the decay of mesons. Accordingly, the study of prompt photons involves processes where the initial state is actually composed of quarks and gluons, and QCD is needed to compute the relevant matrix elements. It is this electromagnetic signature which is generally considered to be useful in collider experiments at RHIC or LHC, as meson decay photons overwhelm the total contribution by several orders of magnitude, and are often suppressed by applying isolation cuts.

In the next section, we will first perform the LO computation for γ production from both direct and fragmentation mechanisms, followed by a discussion of how the choice of energy scales affects the computation. We will then proceed to discuss the complications arising at NLO, before devoting a section to the theoretical modifications necessitated by the implementation of isolation criteria. This will be followed by a presentation of the results for the isolated NLO cross-section, compared to experimental data from the LHC. In the final section, we will extend our results to the computation of hadronic cross-sections. The interested reader can find further background material on prompt photon production in [40], or, more recently, in [57].

3.2 Leading-Order Photon Production

3.2.1 Computing the LO cross-section

The most natural way to begin is to enumerate the possible processes that contribute to photon production at leading order (i.e.: order $\alpha_s\alpha$). These are given by $q + \bar{q} \rightarrow \gamma + g$ and $q(\bar{q}) + g \rightarrow \gamma + q(\bar{q})$ and diagrammed in Figure 3.1. Although we will see that the LO contribution lacks precision, it serves as a good starting point to understand the more subtle aspects of the NLO calculation.

The corresponding amplitudes for the LO diagrams are computed using the QCD Feynman rules described in Appendix A, and are given by:

$$\frac{d\hat{\sigma}_a}{d\hat{t}} = \frac{\pi\alpha\alpha_s}{\hat{s}^2} \frac{8}{9} e_q^2 \left(\frac{\hat{u}}{\hat{t}} + \frac{\hat{t}}{\hat{u}} \right) \quad (3.1)$$

$$\frac{d\hat{\sigma}_c}{d\hat{t}} = -\frac{\pi\alpha\alpha_s}{\hat{s}^2} \frac{1}{3} e_q^2 \left(\frac{\hat{u}}{\hat{s}} + \frac{\hat{s}}{\hat{u}} \right) \quad (3.2)$$

In these expressions, e_q^2 refers to the fractional quark charge, $-\frac{1}{3}$ for d and

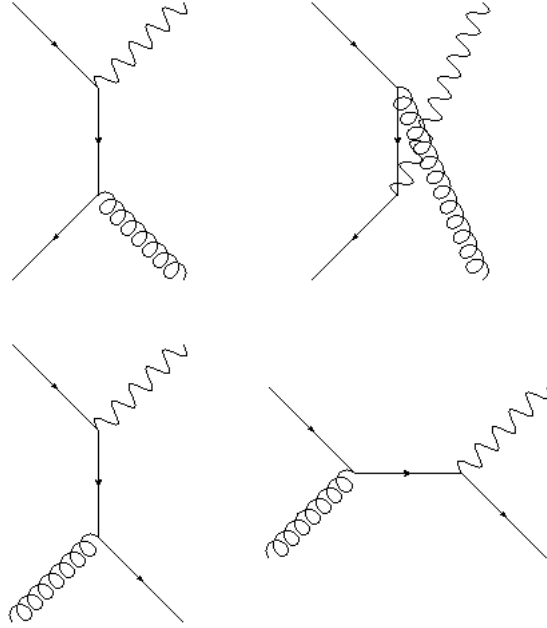


Figure 3.1: LO partonic processes for photon production. The top two diagrams represent quark-antiquark annihilation; the bottom diagrams represent the QCD Compton process

s quarks, and $+\frac{2}{3}$ for u quarks. The coupling α_s is running and given by Eq. 2.22. There is a third permitted tree-level process that generates γ 's, given by $q + \bar{q} \rightarrow \gamma + \gamma$, but, since it scales as $\alpha^2 \sim \frac{1}{10}\alpha_s\alpha$, it is significantly suppressed in comparison, so we do not take it into consideration.

To obtain the total direct cross-section, we convolve these expressions about the proton PDFs, and note that no FFs will play a role at leading order, since we are considering the contribution arising from the pointlike coupling of quarks and photons, which is described exactly by the $q\bar{q}\gamma$ QED vertex. Accordingly, we can use our discussion of kinematics from Section 2.6 to simplify (2.28) as:

$$\frac{d\sigma_{LO}^{(D)}}{d^2p_T dy} = \sum_{a,b} \int dx_a G_{a/p}(x_a, Q) G_{b/p}(x_b, Q) \frac{1}{\pi} \frac{2x_a x_b}{2x_a - x_T e^y} \frac{d\hat{\sigma}_{ab \rightarrow \gamma d}}{d\hat{t}} \quad (3.3)$$

where $x_T \equiv \frac{2p_T}{\sqrt{s}}$ is the fraction of the hadronic center-of-mass energy carried away by the outgoing photon. $G_{a/p}(x_a)$ is the proton PDF for parton a with momentum fraction x_a . The factor $\frac{1}{\pi} \frac{2x_a x_b}{2x_a - x_T e^y}$ comes about when eliminating the delta functions to express the right-hand-side as an integral over x_a , which also results in the

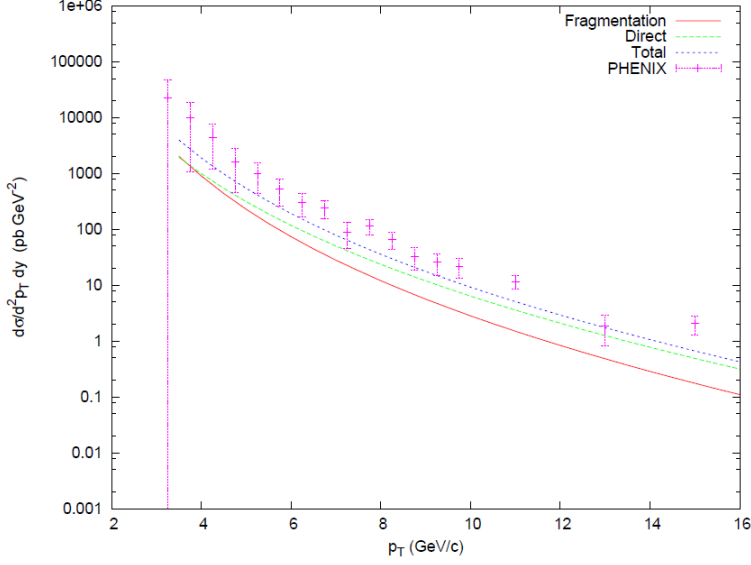


Figure 3.2: LO high- p_T photon spectrum in pp collisions at $\sqrt{s} = 200\text{GeV}$. The data points and error bars are taken from PHENIX.[58] The dashed and solid curves respectively correspond to LO direct and fragmentation γ , and the dotted line is the sum of both contributions. $\mu = Q = Q_F = p_T^\gamma$.

kinematic relation $x_b = \frac{x_a x_T e^{-y}}{2x_a - x_T e^y}$. Setting $x_b = 1$ in the previous expression, we obtain $x_{a,min} = \frac{x_T e^y}{2 - x_T e^{-y}}$, which fixes our integration range. Note that here the final-state parton d is fixed exclusively by a and b in each process, whereas this is generally not the case (hence the sum over only a and b).

In addition to the direct contribution, we must still compute the LO contribution from the fragmentation of a photon from an outgoing hard parton, which we will denote by $\sigma_{LO}^{(F)}$. A similar expression can be derived for it:

$$\frac{d\sigma_{LO}^{(F)}}{d^2 p_T dy} = \sum_{a,b,c,d} \int dx_a dx_b G_{a/p}(x_a, Q) G_{b/p}(x_b, Q) D_{\gamma/c}(z, Q_f) \frac{1}{\pi z} \frac{d\hat{\sigma}_{ab \rightarrow cd}}{d\hat{t}} \quad (3.4)$$

with the kinematic constraint $z = \frac{x_T}{2} \left(\frac{e^{-y}}{x_b} + \frac{e^y}{x_a} \right)$. Here, $D_{\gamma/c}(z, Q_f)$ is the appropriate photon fragmentation function, dependent on the fragmentation scale Q_f , and the momentum fraction z of the photon with respect to the fragmenting parton. As before, the integration boundaries are also fixed by kinematics and are given by: $x_{a,min} = \frac{x_T e^y}{2 - x_T e^{-y}}$ and $x_{b,min} = \frac{x_a x_T e^{-y}}{2x_a - x_T e^y}$. It is interesting to note that, even at LO, the expression (3.4) contains a whopping 127 terms when using three

flavors of quark, since the photon FF can be convolved with any partonic process of order α_s^2 .

In this case, we have numerically evaluated the results of Equations (3.3) and (3.4) at midrapidity ($y = 0$), as well as the total LO cross-section, which is simply their sum, and plotted these as a function of p_T in Figure 3.2. The proton PDFs used here are obtained from the CTEQ5 LO parameterization [42], while the γ FFs are extracted from data from $e^+ + e^-$ collisions using the Vector Dominance Model (VDM) approach [48]. We have set the energy scales as $\mu = Q = Q_F = p_T^\gamma$. The CM energy is taken to be $\sqrt{s} = 200\text{GeV}$, corresponding to RHIC settings, and experimental error bars from current PHENIX data is overlaid on the theoretical plot. It is clear upon examination that the bare LO result is not entirely sufficient to describe experimental data – for most of the p_T range, the observed cross-section is approximately 2-3 times greater than what has been calculated.

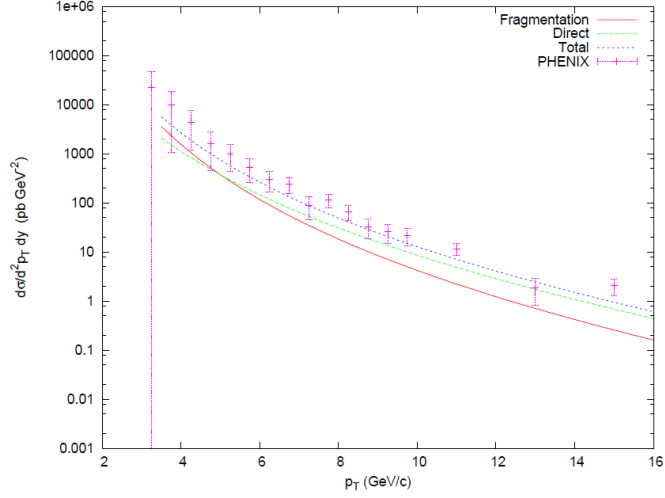
Since the LHC performs measurements of *isolated* photons, which are only introduced in Section 3.4, we will postpone a comparison to these results for that section. Before moving to the NLO computation, we now briefly consider if altering the various scale dependences in the LO calculation can affect the result in any meaningful way.

3.2.2 Modifying our scale dependences

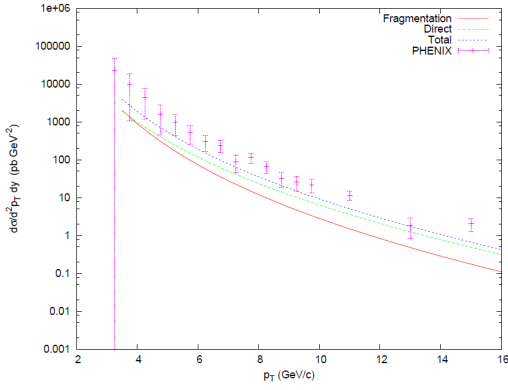
The reader may have noticed that we “cheated” a bit by arbitrarily choosing the relevant scales in the calculation to all be equal to p_T . As detailed in Section 2.5, although these scales must formally be of the same order of magnitude, they can still vary by a constant of order 1. In practice, this can allow for a significant variation in the computed cross-sections.

To illustrate this, in Figure 3.3 we compare our LO result for the cases in which we set our scales Q , Q_F and μ all to be equal to $p_T/2$, p_T , and $2p_T$. This is of course not an exclusive choice, as there is the possibility to modify the scales independently of one another as well. In-depth studies of different factorization prescriptions can be found in [53, 54] and references therein. In Figure 3.3d, we present the ratio of curves with scales set to $p_T/2$ and $2p_T$ to the original curve whose scales are set to p_T .

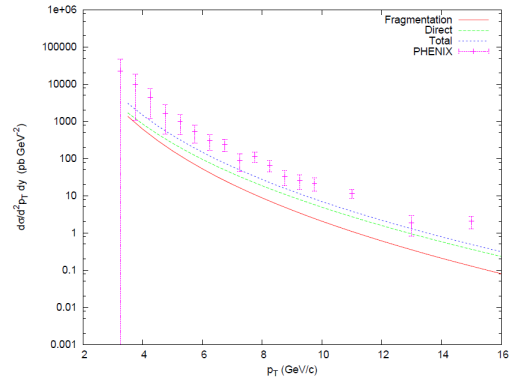
Most importantly, we note in Figure 3.3d that modifying the scales by an $\mathcal{O}(1)$



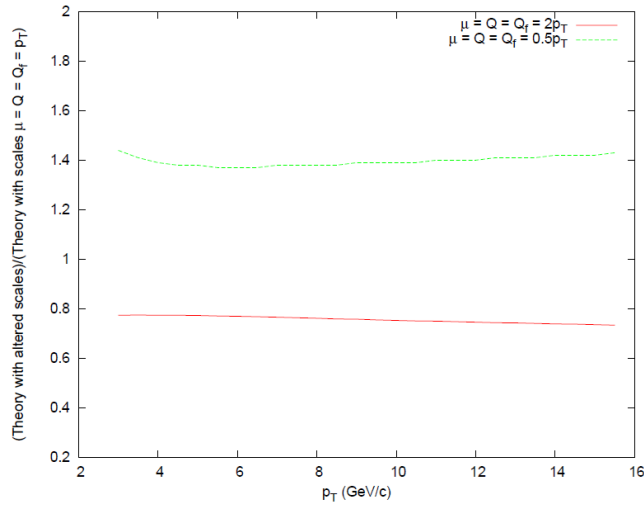
(a) $p_T/2$



(b) p_T



(c) $2p_T$



(d) Effect of modifying scales

Figure 3.3: LO high- p_T photon spectrum in pp collisions at RHIC, calculated at various scales. The data points and error bars are taken from PHENIX.[58] The bottom subfigure plots the ratio of the curves with scales $p_T/2$ and $2p_T$ to the curve with scales set to p_T .

constant can affect the original result in Fig. 3.2 by an approximate factor of 0.8-1.4. In other words, going from scale settings of $2p_T$ to $p_T/2$ at LO induces a multiplicative correction of almost 2 – the theoretical uncertainty due to scales is almost as large as the value of the cross-section itself! This in itself offers one of the most important reasons for going to NLO : we expect theoretically that when NLO terms are retained, these scale dependences will be reduced, since any such factorization scale alteration is compensated for by the inclusion of NLO “direct” terms which contain subleading logarithms.

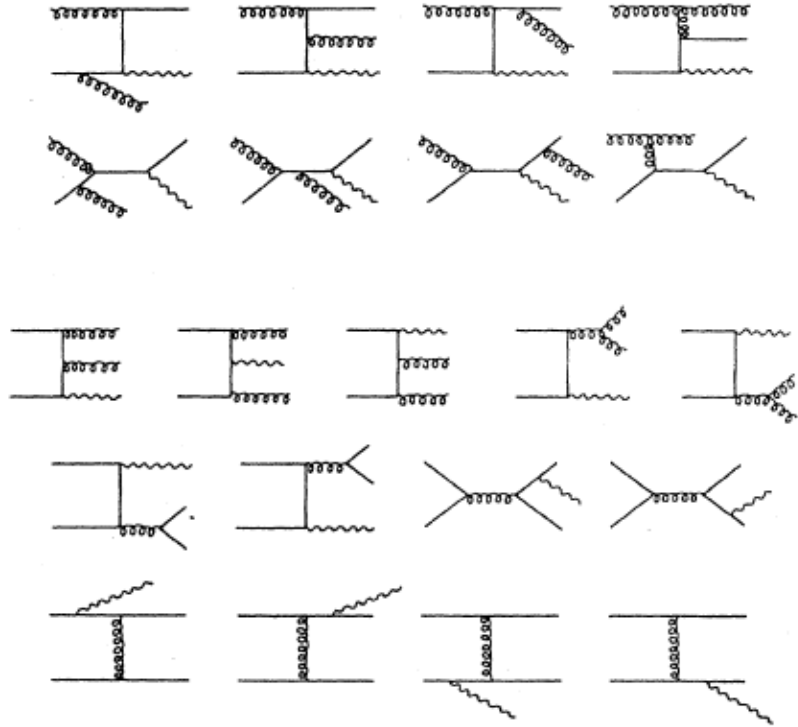
We can also note that the results with scales set to $p_T/2$ (Fig. 3.3a) seem to give the best results, with a curve that generally fits into the error bars. It is too optimistic for us to claim that this implies the success of LO pQCD for this calculation, in light of the aforementioned factor of 2 that can be induced by modifying the scale – this factor is of the same order as the K -factor that we would expect from including the NLO correction. We can also note that the experimental data from PHENIX is somewhat poorly constrained – when we later look at LHC results, we will see that the LO result is quite far off from accurately reproducing the experimental data.

3.3 NLO Photon Production

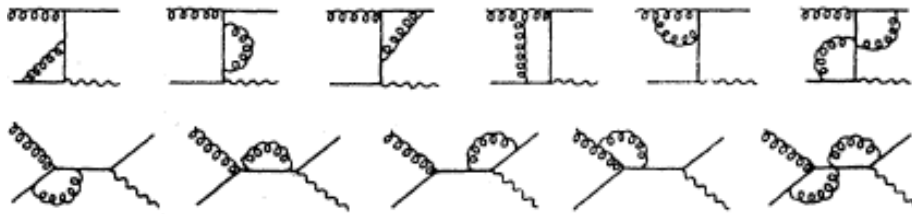
At NLO in α_s , there are a significantly larger number of QCD diagrams that produce direct photons than at LO. Essentially, for any parton-parton tree diagram of order α_s^2 which has a quark or antiquark leg, we are able to attach a photon. In addition, we must consider the interference of one-loop diagrams of order g^3e with our Born diagrams (the product of which gives a cross-section contribution of order $\alpha_s^2\alpha$), in order to cancel the soft divergences in our cross-sections. A few examples of these types of diagrams are illustrated in Figure 3.4, borrowed from [59].

The reader should recall that we explicitly computed this type of NLO correction Chapter 2 for the process $qq \rightarrow qq\gamma$. It is useful to refer back to this if one wishes to calculate the specific functional forms that the matrix elements and the phase space will take at NLO.

In addition to the direct contribution, there are NLO fragmentation photons



(a) $2 \rightarrow 3$ processes



(b) One-loop corrections

Figure 3.4: A few examples of NLO photon production diagrams. Both tree-level processes with an extra final-state particle as well as $2 \rightarrow 2$ one-loop processes must be taken into account to eliminate soft divergences. The diagram is modified from an illustration in [59].

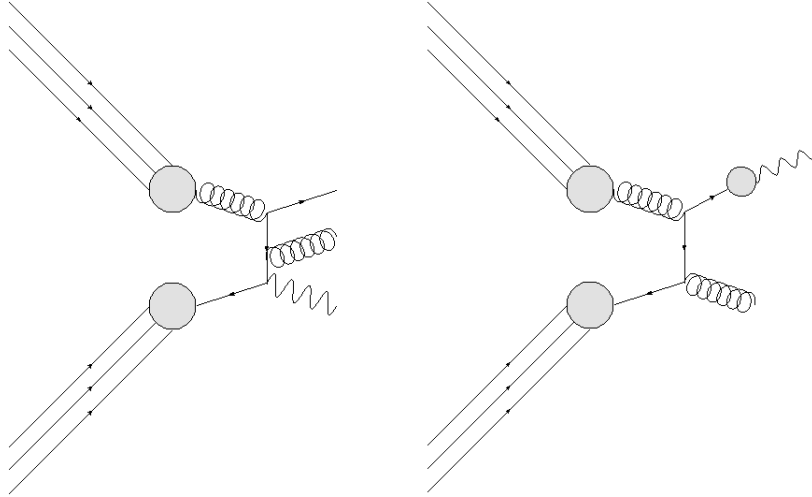


Figure 3.5: On the left, we have a typical NLO diagram for “direct” γ production, while, on the right, we have a typical diagram for the LO fragmentation γ contribution. The grey circles represent non-perturbative processes, given by the PDFs and FFs in the initial state and final state respectively. Both diagrams are of order $\alpha_s^2\alpha$.

arising from the $2 \rightarrow 3$ parton-parton processes in which one of the final-state partons fragments into a γ . Again, because of the fragmentation vertex’s anomalous dependence on α_s , we expect this contribution to be of the same order as the NLO direct γ ’s. To arbitrary order, we are able to write out the generalized version of Equation (2.29) for the total hard photon cross-section:

$$\frac{d\sigma}{dp_T^\gamma dy_\gamma} = \frac{d\sigma_\gamma}{dp_T^\gamma dy_\gamma}(p_\gamma; \mu, Q, Q_F) + \sum_c \int_0^1 \frac{dz}{z} \frac{d\sigma_c}{dp_T^\gamma dy_\gamma}\left(\frac{p_\gamma}{z}; \mu, Q, Q_F\right) D_c^\gamma(z; Q_F) \quad (3.5)$$

where σ_γ is the total “direct photon” cross-section and σ_c is the cross-section for producing final-state jet c , whose convolution about the γ FF gives the “fragmentation” cross-section. Our liberal use of quotation marks here is not solely for sarcastic effect: in fact, it is important to remember that, although we have made an obvious distinction between these two contributions – direct and fragmentation – at LO, at arbitrary order it is only the *sum* of these contributions that is a physical observable. This can be intuitively illustrated by considering Figure 3.5. Although the hard photon is produced through two different processes, they both contribute at the same order in the expansion in α_s , and the only reason they are “drawn differently” has to do with an arbitrary choice we made about the scale

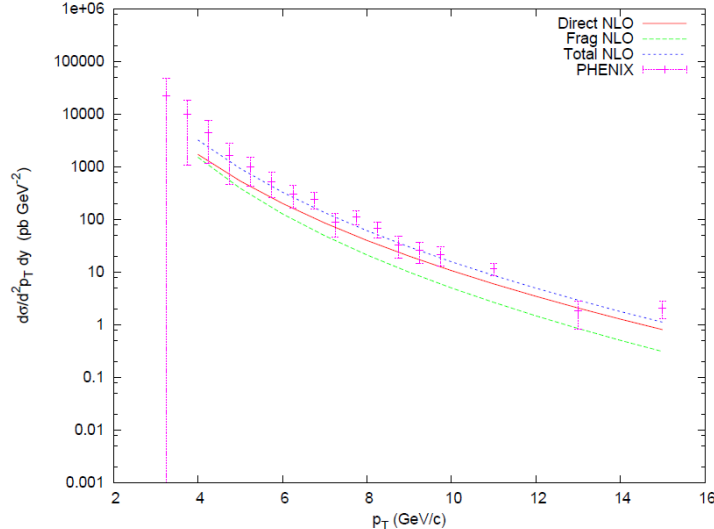


Figure 3.6: NLO High- p_T photon spectrum in pp collisions at $\sqrt{s} = 200\text{GeV}$. The data points and error bars are taken from PHENIX.[58] The dashed and solid curves respectively correspond to NLO direct and fragmentation γ , computed in JETPHOX, and the dotted line is the sum of both contributions. $\mu = Q = Q_F = p_T^\gamma$.

Q_F .

Using JETPHOX [35, 36], we’ve evaluated (3.5) at order $\alpha_s^2\alpha$. In the computation, we used the NLO CTEQ6 PDFs [42], calculated in the \overline{MS} factorization scheme, and Set II of the photon FFs from Bourhis, et al [48]. We’ve once again selected the scales $\mu = Q = Q_F = p_T^\gamma$, and chosen the kinematic range $-0.35 < y < 0.35$ and $4\text{GeV} < p_T^\gamma < 15\text{GeV}$. The results are plotted in Figure 3.6, and the K -factor obtained by taking the quotient of the NLO and LO results is given in 3.7a.

We are able to observe that the obtained K -factor does not vary significantly over the kinematic range – the values range from 1.56 to 1.69. One can also consider two separate K -factors for the direct and fragmentation components, as in Figure 3.7b, in which case one obtains values that are also approximately constant. Although we’ll later see that these factors are not completely sufficient in describing NLO corrections to two-particle correlations, it is still remarkable that they should work as well as they do in the single- γ case – both the phase space and matrix elements obtained in the LO and NLO computations take on completely different forms, so it is not at all evident that the final result should possess the same functional form for the given kinematic range.

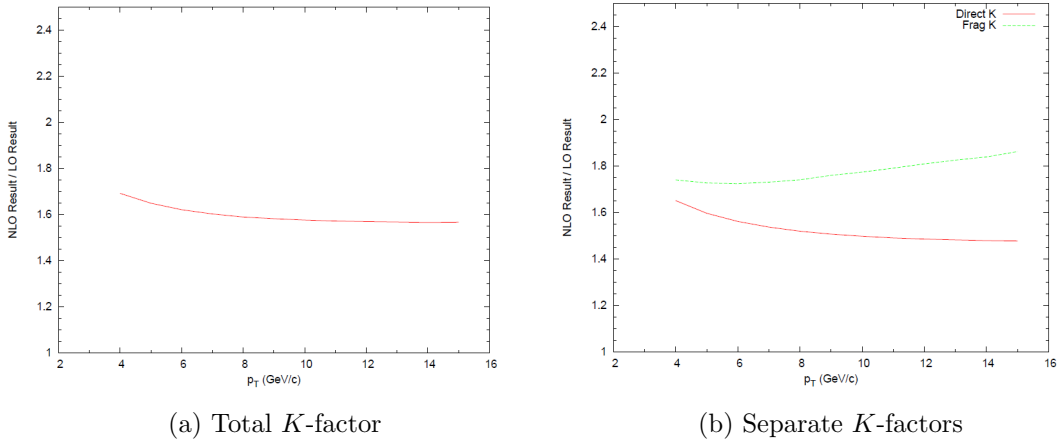


Figure 3.7: K -factors for photon production in the kinematic range $4\text{GeV} < p_T^\gamma < 15\text{GeV}$. The left diagram is the total ratio of NLO to LO computations, while the right diagram contains separate K -factors for direct and fragmentation contributions.

Although we are now prepared to extend our NLO formalism to LHC energies, the CMS detector does not in fact detect *inclusive* cross-sections – experimental isolation criteria are applied which alter the computation. Accordingly, we take a brief detour to discuss these effects.

3.4 Isolation Criteria

3.4.1 Introduction

Ideally, we could just numerically evaluate the NLO expressions for the direct and fragmentation cross-sections to obtain a reasonably precise prediction for hard photon production in pp collisions. Experimentally, however, there is also an enormous γ background from meson decay processes (most commonly $\pi_0 \rightarrow \gamma\gamma$ or $\eta \rightarrow \gamma\gamma$) that overwhelms the prompt signal by several orders of magnitude. It is particularly difficult to experimentally discriminate between prompt and decay photons owing to the fact that the outgoing decay- γ pair is often severely Lorentz contracted, so that it registers in the detector as a single γ .

Accordingly, experimentalists need to apply certain *isolation criteria* that can selectively remove these unwanted signatures from the experimental data. Unfortunately, one cannot apply these isolation cuts without removing part of the prompt photon cross-section, so that the theoretical calculation needs to be cor-

respondingly modified. We can understand this better by actually describing one of the main isolation algorithms used. When a photon with rapidity y_γ and azimuthal angle ϕ_γ is detected, we define an *isolation cone* in $\phi - y$ space around the photon, which is described by the volume:

$$(y - y_\gamma)^2 + (\phi - \phi_\gamma)^2 \leq R^2 \quad (3.6)$$

where R is the cone radius. Inside the cone, we require that the total hadronic energy satisfies:

$$E_T^{had} \leq E_T^{max} \quad (3.7)$$

where E_T^{max} is some limiting transverse energy that can either be constant, or a fraction ϵ_h of the photon's transverse momentum. This criterion is not unique – for example, another common choice is given in [60]. While the signal from meson-decay photons will be removed for a good choice of parameters, fragmentation photons also emerge as part of a collimated jet of hadrons and so will be largely suppressed by the imposed criterion. Direct photons will usually emerge in a region of low hadronic density and so will not be removed, although NLO effects do bring about a slight suppression.

In the following subsections, we more quantitatively examine how theoretical cross-sections for both fragmentation and direct γ 's need to be modified when an isolation criterion is applied, and then use these results to compute the NLO isolated prompt photon cross-section, which we then compare to CMS data.

3.4.2 Isolated fragmentation photons

It is important to recognize that not all fragmentation photons will be suppressed by the criterion given in (3.6) and (3.7). If we consider a LO process in which a final-state parton fragments into a γ , as in Figure 3.8a, then the total energy in the cone will be given by $E_\gamma + E_{frag}$. We can combine $E_\gamma = zE_c$ and $E_{had} = E_{frag} = (1 - z)E_c$ with the criterion (3.7) to obtain:

$$z > z_c \equiv \frac{1}{1 + \epsilon_h} \quad (3.8)$$

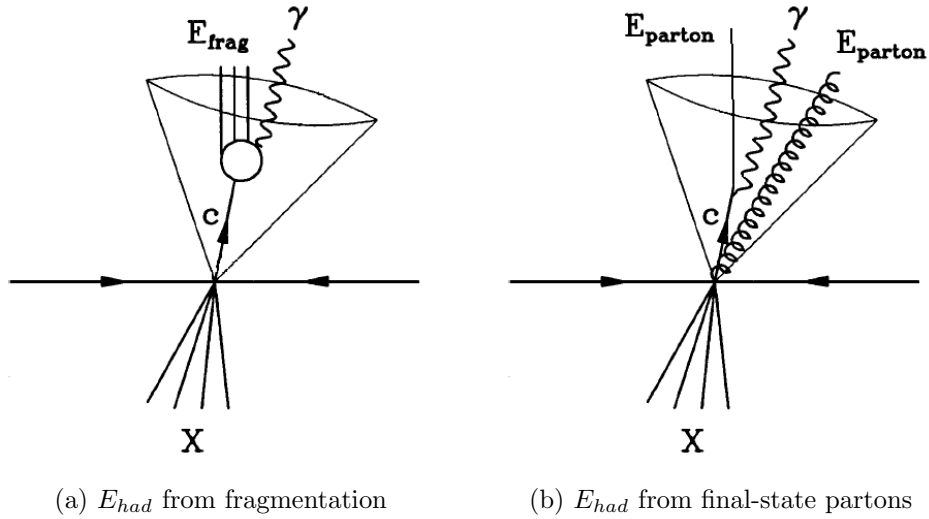


Figure 3.8: A schematic of how final-state hadronic energy may originate from the fragmentation process at LO (left), and from extra final-state partons at NLO (right). The pictures are adapted from one used in [61].

In plain language, if the γ emerges carrying away almost all of the energy of the fragmenting parton (more precisely, carrying momentum fraction $z > z_c$), it will avoid suppression. Nevertheless, for a choice of order $\epsilon_h = 0.1$, all contributions with $z < 0.91$ – a significant majority – will be removed. Accordingly, although the isolation criteria requires that we modify our theoretical calculation, we observe that it has the added benefit of removing a great deal of the uncertainty due to the theoretical uncertainty in the FFs $D_{q/\gamma}$ and $D_{g/\gamma}$. The cross-section (Eq. (3.5)) is correspondingly modified as:

$$\frac{d\sigma^{iso}}{dp_T^\gamma dy_\gamma} = \frac{d\sigma_\gamma}{dp_T^\gamma dy_\gamma}(p_\gamma; \mu, Q, Q_F) + \sum_c \int_{z_c}^1 \frac{dz}{z} \frac{d\sigma_c}{dp_T^\gamma dy_\gamma}\left(\frac{p_\gamma}{z}; \mu, Q, Q_F\right) D_c^\gamma(z; Q_F) \quad (3.9)$$

It's important to note that this simple treatment relied on the fact that the “fragmentation cone” (i.e.: the cone determined by Q_F which describes the boundary in phase space within which collinear partons are absorbed into the relevant FFs) lies entirely within the isolation cone. In this analysis, when numerically evaluating results using the PHOX programs, a value of $R_T = 0.1$ was always selected, while the experimentally defined isolation cones were of the order $R \sim 0.3 - 0.4$, rendering such a treatment acceptable.

3.4.3 Isolated direct photons

While at LO the only possible source of hadronic energy in the isolation cone could be from the fragmentation process, at NLO we must take into account the fact that in $2 \rightarrow n$ processes, with $n \geq 3$, the extra final-state partons carry their own hadronic energy contribution. If any of the extra partons are sufficiently collinear to the photon so that they fall within the isolation cone (but are still well-separated enough that the process is part of the “direct” perturbative contribution), then the criterion will be violated if $E_{parton} > \epsilon_h E_\gamma$. This is heuristically illustrated in Figure 3.8b.

Although the PHOX programs take isolation effects into account internally, the programs are unable [62] to compute two-particle cross-sections with a single isolated leg. In theory, this does not affect the computations for this chapter, since we are dealing with single-particle cross-sections here; however, we will need an alternate method for Chapter 4, which deals with two-particle spectra. Accordingly, we adopt here an approximate method outlined in [61] which gives an order of magnitude estimate for the effect of isolation on direct γ 's. We will ultimately find that this effect is negligible for the set of experimental parameters in usage here.

Firstly, we can separate our direct cross-section into LO and higher-order (HO) terms, the former of which is unaffected by isolation, and the latter of which we write as the difference of an *inclusive* term and a *subtraction* term:

$$d\sigma_\gamma^{iso} = d\sigma_\gamma^{LO,incl} + [d\sigma_\gamma^{HO,incl} - d\sigma_\gamma^{HO,sub}] \quad (3.10)$$

The phase space for the subtraction term corresponds to the phase space for finding one of the final-state partons in the isolation cone with energy between $\epsilon_h E_\gamma$ and some maximum energy \mathcal{E} fixed by kinematics:

$$\frac{d^3k}{(2\pi)^3 2E} = \frac{1}{(2\pi)^3} \int_\delta d\Omega \int_{\epsilon_h E_\gamma}^{\mathcal{E}} \frac{EdE}{2} \quad (3.11)$$

Here, we've adopted the convention that, for computations at midrapidity (for which $y_\gamma \approx y = 0$), we can describe the isolation cone in terms of its half-angle opening δ in ϕ -space, so that $R \approx \delta$.

Next considering the change in the appropriate squared matrix elements, we can foresee a possible issue before even writing anything down: the elimination of IR divergences depended on the precise cancellation of $2 \rightarrow 3$ *inclusive* terms and $2 \rightarrow 2$ loop diagrams. Since the isolation cut restricts the phase space of the former (but not of the latter), we cannot expect this cancellation to occur in the same way. Accordingly, we want to specifically consider the case in which ϵ_h is very small, so we can isolate the case in which a soft gluon enters the isolation cone and consider what effect this might have.

When we consider the limit in which $\epsilon_h \rightarrow 0$, under the soft gluon approximation [63, 64] we can approximate our $2 \rightarrow 3$ matrix element as a convolution over the Born expression :

$$d\sigma_\gamma^{HO,sub} \approx g^2 \frac{1}{(2\pi)^3} \int_\delta d\Omega \int_{\epsilon_h E_\gamma}^\epsilon \frac{E dE}{2} \left(\frac{1}{E^2} \right) C(p_\gamma, x_1, x_2) d\sigma_\gamma^{LO,incl} \quad (3.12)$$

where $C(p_\gamma, x_1, x_2)$ is a function of the color factors and the momenta of the incoming and outgoing partons (excluding the gluon itself). The $1/E^2$ factor is a general factor present in the squared matrix element for soft gluon emission. We can easily perform this integral to obtain:

$$d\sigma_\gamma^{HO,sub} \approx \Gamma(p_\gamma, x_1, x_2, \delta, \epsilon) d\sigma_\gamma^{LO,incl} \quad (3.13)$$

with:

$$\Gamma(p_\gamma, x_1, x_2, \delta, \epsilon) \equiv \left(\frac{\alpha_s}{\pi} \right) \sin^2 \left(\frac{\delta}{2} \right) \log \left(\frac{1}{\epsilon_h} \right) C(p_\gamma, x_1, x_2) + \mathcal{O}(\epsilon^0) \quad (3.14)$$

We are now able to use (3.13) and (3.14) to modify (3.9), giving us the final expression for the NLO prompt photon cross-section, taking into account the effect of the isolation criterion on both direct and fragmentation components:

$$\begin{aligned} \frac{d\sigma^{iso}}{dp_T^\gamma dy_\gamma} &= [1 - \Gamma(p_\gamma, x_1, x_2, \delta, \epsilon)] \frac{d\sigma_\gamma^{LO}}{dp_T^\gamma dy_\gamma}(p_\gamma; \mu, Q, Q_F) \\ &+ \frac{d\sigma_\gamma^{HO}}{dp_T^\gamma dy_\gamma}(p_\gamma; \mu, Q, Q_F) + \sum_c \int_{z_c}^1 \frac{dz}{z} \frac{d\sigma_c}{dp_T^\gamma dy_\gamma} \left(\frac{p_\gamma}{z}; \mu, Q, Q_F \right) D_c^\gamma(z; Q_F) \end{aligned} \quad (3.15)$$

While, in the following section, JETPHOX will be used to numerically evaluate $d\sigma_\gamma^{NLO}$, so that the approximation (3.12) is unnecessary, our final result (3.15) will be used directly in Chapter 4 since in this case DIPHOX is no longer able to evaluate the exact result.

3.4.4 Results

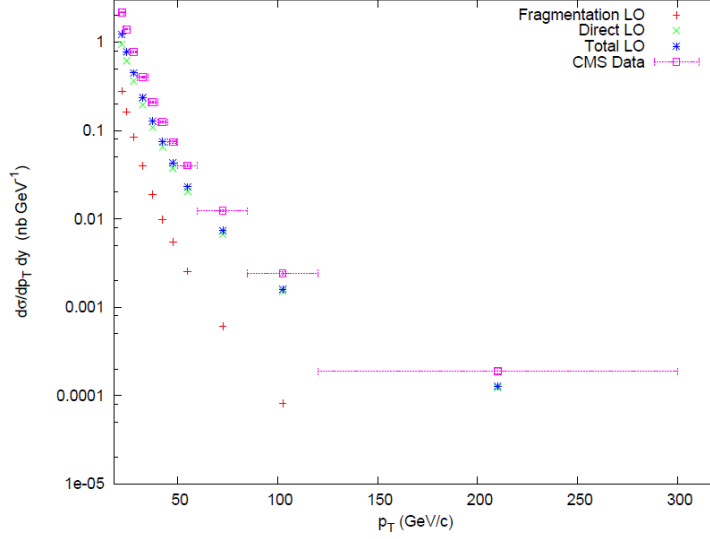
In this section, we are finally prepared to present results for the isolated NLO cross-section, as compared to CMS data. In this case, the experimental cone energy is given as a constant, rather than a multiple of E_γ , which in our earlier treatment simply requires the substitution $\epsilon_h \rightarrow \frac{E_T^{max}}{E_\gamma}$ in Equation (3.8). Specifically, the CMS isolation criteria are given by $R = 0.4$ and $E_T^{max} = 5GeV$.

For our computation, we once again use the NLO PDFs given by the CTEQ6 collaboration, obtained in the \overline{MS} scheme, and the photon FFs from the Bourhis set. We choose our scales so that $\mu = Q = Q_F = p_T^\gamma$, and set $\sqrt{s} = 7000GeV$, corresponding to the current LHC operating energy. We apply the constraints $-2.5 < y_\gamma < 2.5$ and $21GeV < p_T^\gamma < 300GeV$, corresponding to the kinematic cuts used in the study [65]. The results are plotted in Figure 3.9.

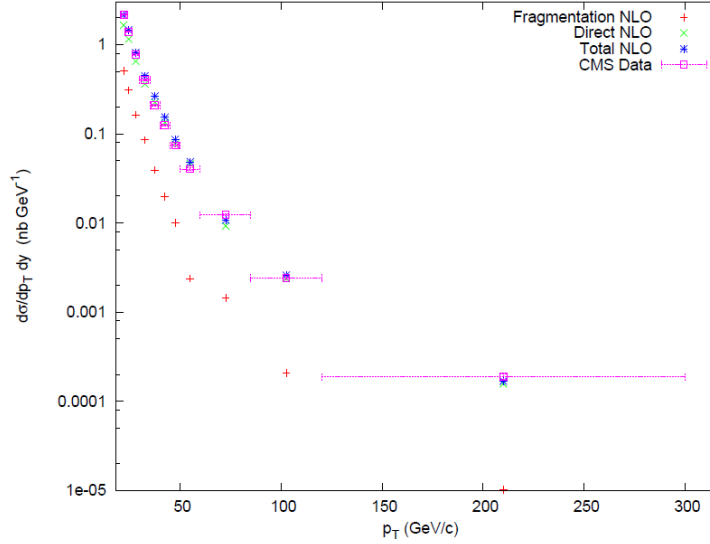
We observe in Figure 3.9a that even once the isolation criterion is applied, the LO result for prompt photon production at $\sqrt{s} = 7000GeV$ does not sufficiently account for experimental results. It is approximately half of the observed cross-section. In Figure 3.9b, we add in the NLO contribution, and observe a much better agreement with data.

In contrast to the RHIC data for inclusive photon production, for which the fragmentation and direct contributions were approximately the same for the majority of the kinematic range, we observe that here the experimental isolation criterion suppresses the fragmentation contribution by almost an order of magnitude at both LO and NLO.

As before, we can also briefly study the effect of modifying the scales at NLO, illustrated in Figure 3.10. Here, we've plotted the same cross-section as in Figure 3.9b in both the cases where the scales have been doubled and halved, as well as the ratio of these cross-sections with respect to our earlier result. We see that, in general, the modified results are within 10% of the original result, although, not surprisingly, for the larger p_T bins the difference becomes much larger.



(a) LO pQCD Result



(b) NLO pQCD Result

Figure 3.9: High- p_T isolated photon spectrum in pp collisions at $\sqrt{s} = 7TeV$. The data points and error bars for each bin are taken from CMS.[65] The green and red crosses respectively correspond to isolated direct and fragmentation γ 's for each bin, computed in JETPHOX, and the stars are the sum of both contributions. $\mu = Q = Q_F = p_T^\gamma$

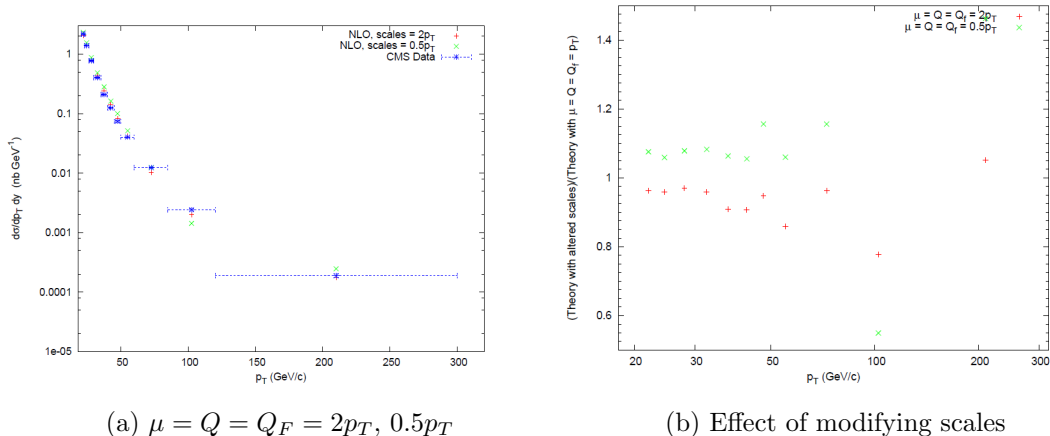


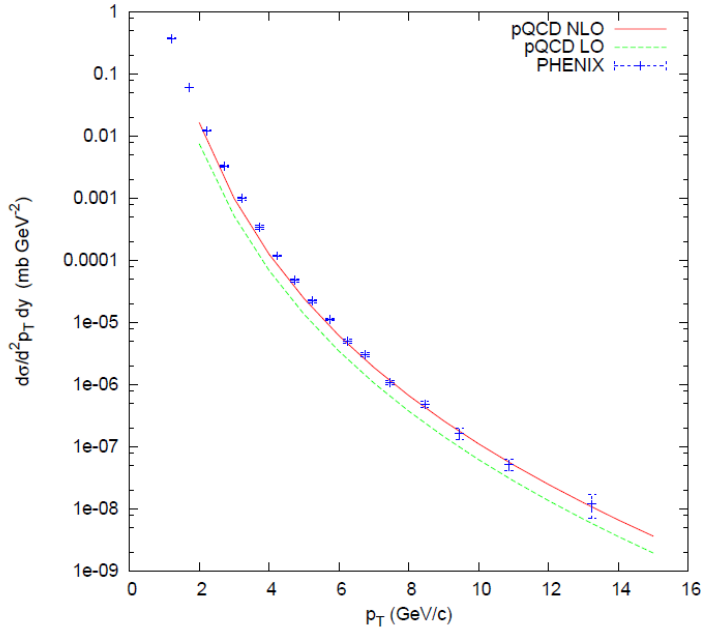
Figure 3.10: High- p_T isolated photon spectrum in pp collisions at $\sqrt{s} = 7TeV$, calculated at NLO, with scales set to $\mu = Q = Q_F = 2p_T^\gamma$. On the right, we take the ratio of the result with the new scale to the result from Figure 3.9b.

3.5 Hadron Production

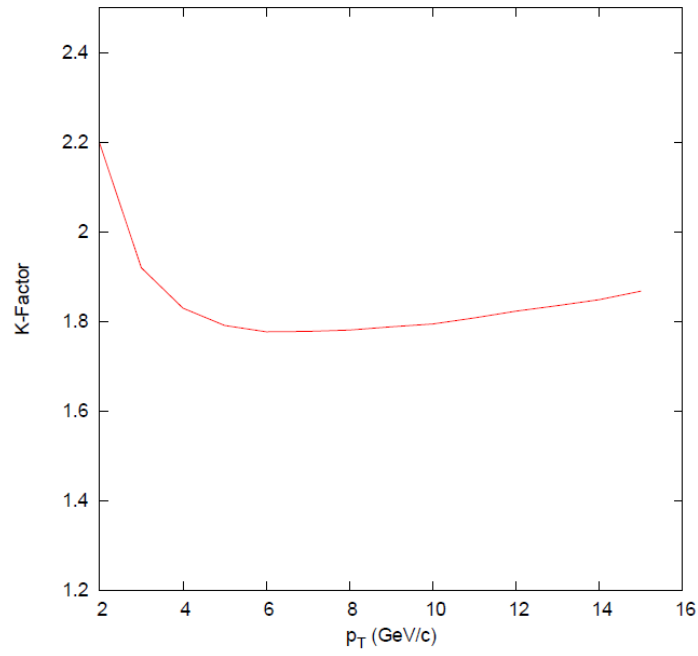
Before concluding this chapter, we will give some of the quantitative results for the production of hadrons in pp collisions, and in particular the differential cross-sections of neutral pion production. These are relevant in the context of the $\gamma - \pi$ correlation cross-sections computed in Chapter 4. Since the theoretical basis of these calculations is virtually the same as in the case of photons, we will focus principally on the comparison of theory to experimental results.

In fact, the only differences to note with respect to our earlier cross-section computations with photons are:

- The lowest order partonic diagrams are of order α_s^2 (instead of α_s) in the strong coupling. Therefore, our LO computation will emulate the LO calculation of fragmentation γ 's (i.e.: Equation (3.4)), with the pion FF $D_{\pi_0/c}$ substituted for $D_{\gamma/c}$.
- There is now a little more ambiguity in the choice of scales, since we can consider either the p_T of the jet or the fragmented pion, which can vary by up to an order of magnitude.
- Pion events generally have a very low background signal, so that no isolation or other selection criteria need to be imposed that could modify the theoretical calculation.



(a) pQCD Result



(b) K -factor

Figure 3.11: High- p_T pion spectrum in pp collisions at RHIC, calculated at LO and NLO. The data points and error bars are taken from PHENIX.[58] $\mu = Q = Q_F = p_T^\pi$. The bottom subfigure gives the K -factor.

With these points in mind, we plot in Figure 3.11 the LO and NLO results for inclusive π_0 production in $p + p$ collisions at $\sqrt{s} = 200\text{GeV}$. The energy scales are taken as $\mu = Q = Q_F = p_T^\pi$, and the PDFs are taken as previously from the CTEQ6M set. The pion FFs are obtained using the KKP parameterization [47] at NLO.

We can note that the experimental data bars are much more constrained than in the case of photon production. One reason for this is the lack of substantial background events to take into consideration, as was the case with γ 's due to meson decay. In this way, we're able to appreciate much more the level of precision to which an NLO computation reproduces experimental results. In particular, we note that in the LO case, there is generally a substantial contribution missing. As in the case of photon production, it is useful to calculate the resultant K -factor, which is plotted in 3.11b. Throughout the p_T range, this is mostly constant in the range 1.8-1.9, although at very low p_T the computed correction extends to a value of 2.21. In general, even the NLO result slightly underpredicts the data in this lower range, a phenomenon that can be attributed to the production of softer pions from non-pQCD processes.

Ultimately, in both the case of photon production and pion production, we see that NLO pQCD generally provides excellent agreement with data. In the case of photons, it is clear that both the direct and anomalous contribution need to be taken into account to explain the high- p_T spectrum, and that a full NLO treatment reduces the theoretical uncertainty due to scale choice. In addition, a working formalism exists to modify calculations in the presence of an experimental isolation criterion. In the following chapter we continue treating these issues in the context of two-particle correlations.

Chapter 4

Photon-Hadron Correlations

4.1 Introduction

The measurement of two-particle correlations complements and enhances data obtained from single-particle spectra. At the very least, we can use such observables as complementary tests of the validity of NLO pQCD, since these correlations generate new observables that manifest *entirely as a result of higher-order effects*. We will define, for example, the γ -triggered momentum imbalance parameter x_E , whose experimental distributions can only be accounted for by higher-order processes. Recent PHENIX data [66] actually measures this parameter, so that we can actually contrast the accuracy of our LO and NLO predictions.

In addition, it turns out that there are a wealth of specialized applications for two-particle correlations as well. We will take a short look at the γ - γ and γ - π_0 final-state distributions at LHC energies, which characterize part of the reducible background for the Higgs boson, which frequently decays via $H \rightarrow \gamma\gamma$. [10]

There is also a major application with regard to nuclear collisions : Tagging in-medium jets and hadrons with away-side γ 's allows one to constrain the initial jet energy distributions before interaction with the QGP medium, since the γ 's do not experience any energy loss [12]. This allows for a much more constrained measurement of the redistribution in phase space of the initial jet momenta, which could enable one to use experimental data to write down a medium-modified FF for various hadron species.

4.2 Leading-order Photon-pion Cross-section

Applying the formalism of Chapter 2, the LO double inclusive differential cross-section for the production of two jets can be obtained as:

$$\frac{d\sigma}{dy_1 dy_2 d^2\mathbf{p}_{T,1} d^2\mathbf{p}_{T,2}} = \sum_{a,b} \frac{G_{a/p}(x_a, Q) G_{b/p}(x_b, Q) |\bar{M}|^2}{16\pi^2 x_a x_b s^2} \delta^2(\mathbf{p}_{T,1} - \mathbf{p}_{T,2}) \quad (4.1)$$

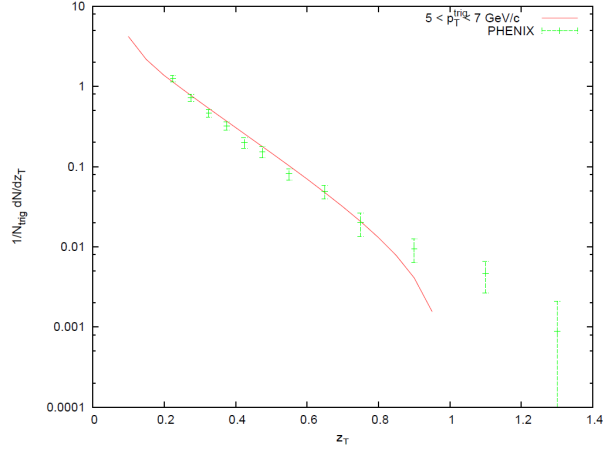
To obtain a photon-hadron cross-section, we treat one jet as our direct γ and consider the fragmentation of the other jet into a given hadron species. Accordingly, we must convolve the above expression about the relevant FF. Substituting in the relevant matrix elements from the processes in 3.1, and making the change of variables $z \equiv p_h/p_\gamma$, we obtain:

$$\frac{d\sigma_{\gamma h}^{(D)}}{d^2p_T dy dz} = \sum_{a,b} \int dx_a G_{a/p}(x_a, Q) G_{b/p}(x_b, Q) D_{h/d}(z, Q_F) \frac{1}{\pi} \frac{2x_a x_b}{2x_a - x_T e^y} \frac{d\sigma_{ab \rightarrow \gamma d}}{d\hat{t}} \quad (4.2)$$

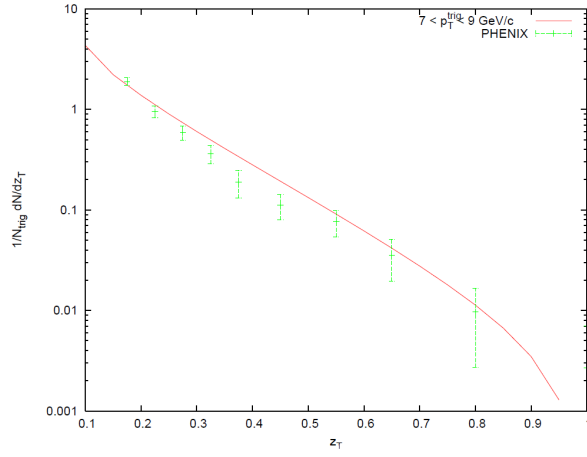
We can note that, as expected, this is the same as the expression (3.3) for LO direct γ 's, convolved about the FF for the away-side hadron $D_{h/d}$. This expression, integrated over the ranges $5\text{GeV} < p_T^{\text{trig}} < 7\text{GeV}$, $7\text{GeV} < p_T^{\text{trig}} < 9\text{GeV}$, and $9\text{GeV} < p_T^{\text{trig}} < 12\text{GeV}$ is plotted in Figure 4.1. In every case, the rapidity ranges of all produced particles are taken to be $-0.35 < y < 0.35$, corresponding to the area subtended by the central arms of the PHENIX detector. The scales are given by $\mu = Q = Q_f = p_T^\gamma$, and the PDFs and FFs are taken from the CTEQ5L and KKP LO sets respectively. The plots are normalized by dividing by the total inelastic cross-section for direct γ 's in the respective kinematic ranges.

We are clearly able to see that, although the data is qualitatively reproduced in all the diagrams for the $z < 0.8$ region, the curve doesn't always fall within accepted error. In addition, at LO it is kinematically impossible to reproduce any results in the regime $z > 1$, since the hadron fragments from a jet whose momentum is the same as the photon's, and therefore has less energy than the photon. The experimental bars in this "LO forbidden" region can almost entirely be attributed to NLO effects, which are discussed in the following section.

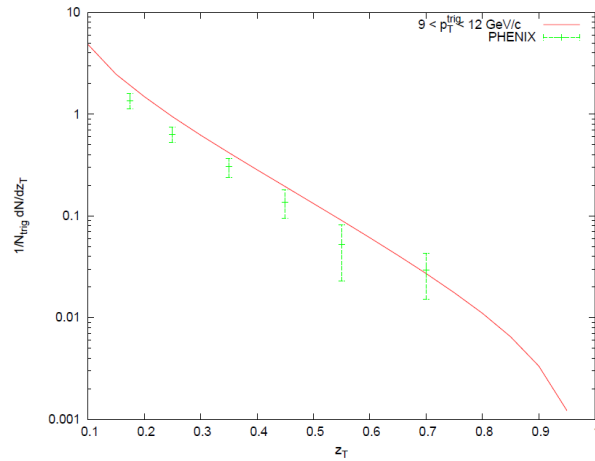
We can also see that there is yet another source of imprecision in our calculation: we have made the approximation that applying isolation cuts allows us to



(a) $5 < p_T^{trig} < 7 \text{ GeV}/c$



(b) $7 < p_T^{trig} < 9 \text{ GeV}/c$



(c) $9 < p_T^{trig} < 12 \text{ GeV}/c$

Figure 4.1: The LO away-side charged hadron yield per isolated direct photon trigger as a function of z for the ranges $5 < p_T^{trig} < 7 \text{ GeV}/c$, $7 < p_T^{trig} < 9 \text{ GeV}/c$, and $9 < p_T^{trig} < 12 \text{ GeV}/c$. The data points and error bars are taken from PHENIX [66] and the curve is calculated using LO pQCD.

considering only the direct γ contribution, and omit any contribution from the channel where both the γ and the hadron fragment. However, from our discussion in Section 3.4, we know that there is a remaining fragmentation contribution in the precise kinematic region where z is large. In the following section, we will attempt to rectify these various inaccuracies and improve upon our results here.

For the sake of completeness, in Figure 4.2, we show the corresponding LO plot calculated at the LHC energy $\sqrt{s} = 7TeV$. We choose all of the same parameters and kinematic constraints as in Subsection 3.4.4, and have separated the results into p_T^γ bins as in [65]. No data currently exists with which to compare these results.

4.3 NLO Cross-section

4.3.1 NLO Observables

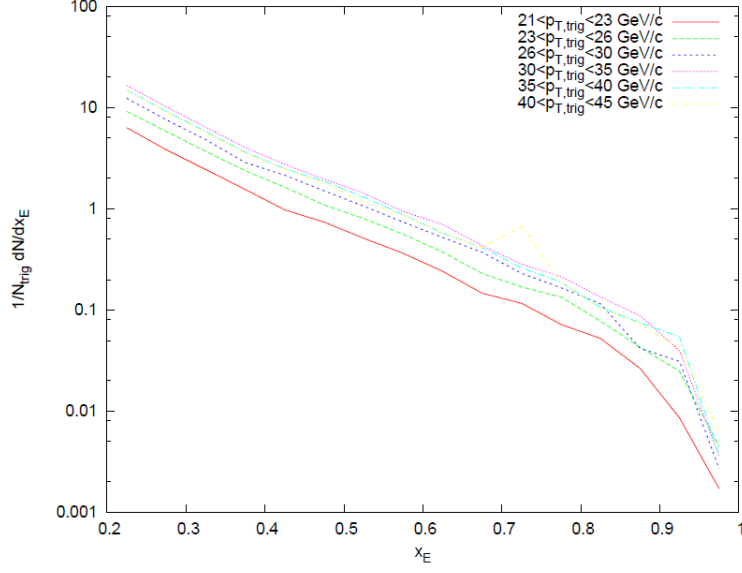
Before presenting our NLO result, we will introduce useful new parameters, and revisit the role of isolation algorithms in the case of two-particle spectra.

At LO, in the case of a direct photon-tagged jet, the parameter $x_h \equiv p_T^{j_1}/p_T^\gamma$ must be equal to 1, as derived in Section 2.6. Accordingly, the momentum fraction of a fragmented hadron is given by $z = p_T^h/p_T^\gamma$. At NLO, we expect that final-state emission will generate an imbalance in the energies of the outgoing particles, as well as introduce additional transverse momenta components. With this mind, we write down the momentum-imbalance parameter for a γ trigger, first defined in [67]:

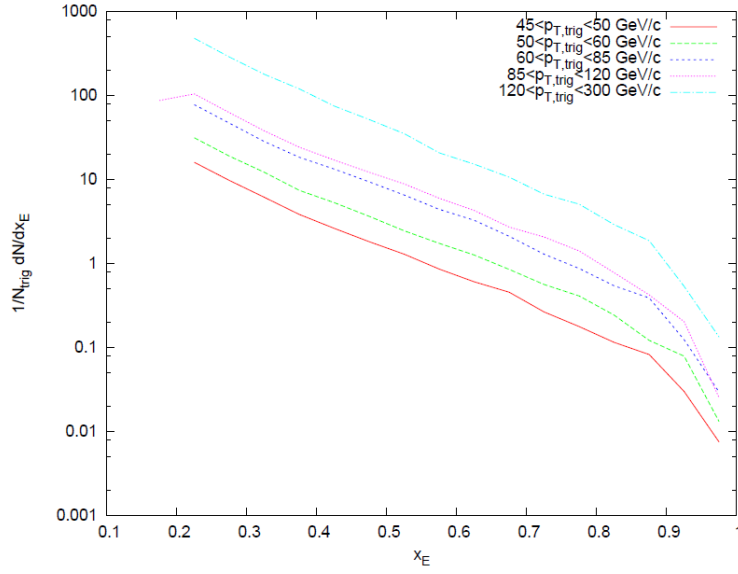
$$x_E \equiv -\frac{\mathbf{p}_{T,\gamma} \cdot \mathbf{p}_{T,h}}{p_{T,\gamma}^2} = -\frac{p_{T,h}}{p_{T,\gamma}} \cos(\Delta\phi) \quad (4.3)$$

In the case $\Delta\phi = \pi$, as at LO, (4.3) just reduces to the expression for z . Experimentally, x_E is easy to measure, as it depends only on the magnitude and direction of the momenta of the outgoing pair. It is, of course, also possible to use triggers other than photons. In [66], for instance, they also measure the experimental yield of π_0 -h pairs with respect to x_E .

We should also note that there are additional reasons a particle pair can gain a non-zero transverse momentum with respect to their outgoing paths. In partic-



(a) $21 < p_T^{trig} < 45 \text{ GeV}/c$



(b) $45 < p_T^{trig} < 300 \text{ GeV}/c$

Figure 4.2: The LO away-side charged hadron yield per direct photon trigger as a function of z for various p_T^γ bins at the LHC.

ular, we mention the so-called “intrinsic k_T effect”, which assumes that the initial colliding partons can have an initial transverse momentum with respect to the colliding hadrons, due to Fermi motion with those hadrons. In general, this effect will be of order $\approx 500 MeV$ [68], and so at higher energies can be almost entirely neglected, as we will do here.

A second useful observable is defined as the vector \mathbf{p}_{out} , whose direction is perpendicular to \mathbf{p}_T^γ and whose magnitude is given by:

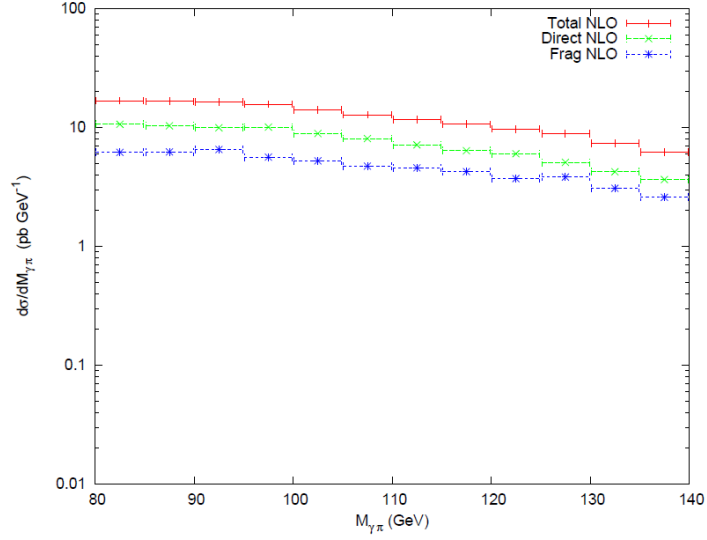
$$p_{out} = p_T^\gamma \sin(\Delta\phi) \quad (4.4)$$

We can note that \mathbf{p}_{out} must purely reflect higher order effects, as LO kinematics ensure that it is always equal to 0. For this reason, this variable is extremely sensitive to the intrinsic k_T effect, which isn’t accounted for in our standard NLO pQCD formalism. At lower energies, it has been shown that NLO pQCD cannot entirely account for this distribution, which requires a resummation of initial-state gluon emission [69].

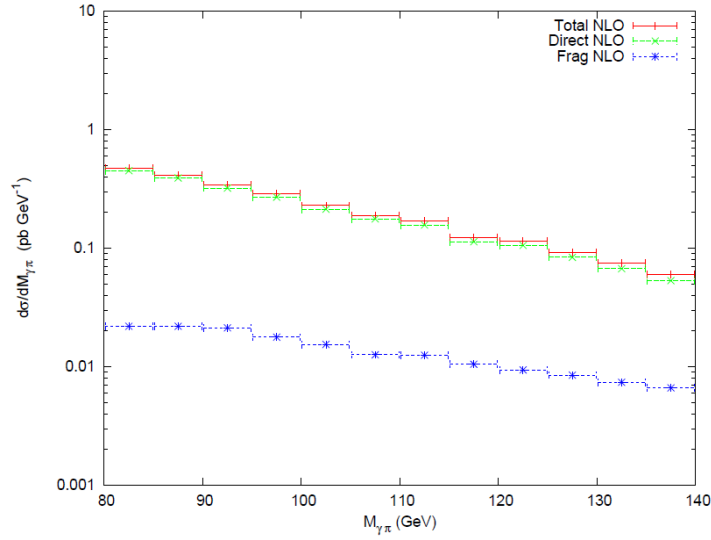
4.3.2 Isolation revisited

As a quantitative example of the extent to which an isolation criterion can affect a two-particle correlation, we consider the two plots in Figure 4.3. In these figures, we’ve plotted the NLO differential cross-section $\frac{d\sigma}{dM_{\gamma\pi_0}}$ against the invariant mass $M_{\gamma\pi_0}$ of a correlated photon-pion pair. This calculation follows a similar study done in [10]. In both subplots, we take the MRST02 PDFs and KKP FFs, and choose our scales as $\mu = Q = Q_F = M_{\gamma\pi_0}/2$. Using the criterion outlined in Section 3.4, we take the radius of the isolation cone as $R = 0.4$. In the top plot, we’ve taken E_T^{max} in the isolation cone to be $100 GeV$, and in the bottom plot to be $10 GeV$.

What must be made clear here is that the isolation criterion is being applied to *both outgoing legs*, with the goal of examining how effective the criterion is in removing the background signal caused by the π_0 decay. It is clear that the isolation cut suppresses a substantial contribution from the total $\gamma - \pi_0$ signal – it is cut by almost 2 orders of magnitude. As usual, we note that at NLO, the subdivision into “direct” and “fragmentation” components is explicitly scale-dependent – however,



(a) $E_T^{max} = 100\text{GeV}$



(b) $E_T^{max} = 10\text{GeV}$

Figure 4.3: Invariant mass distribution for $\gamma - \pi_0$ pairs in the $80 - 140\text{GeV}$ range at $\sqrt{s} = 14\text{TeV}$, with isolation criteria $R = 0.4$ and varying E_T^{max} .

the isolation cone is large enough so that, for any reasonable choice of Q_f , the entire fragmentation component lies in the cone. Meanwhile, in Figure 4.4, we study the effect of isolation on final-state $\gamma - \gamma$ pairs and see that this is affected much less when going to the stronger isolation criterion. The cross-section of direct $\gamma - \gamma$ pairs is virtually unchanged between the top plot ($E_T^{max} = 10GeV$) and the bottom plot ($E_T^{max} = 100GeV$), while the contributions from fragmentation γ -direct γ pairs are reduced by a factor of 0.6-0.8. Fragmentation γ -fragmentation γ pairs are suppressed by 1-2 orders of magnitude so that their contribution to the total cross-section becomes almost negligible.

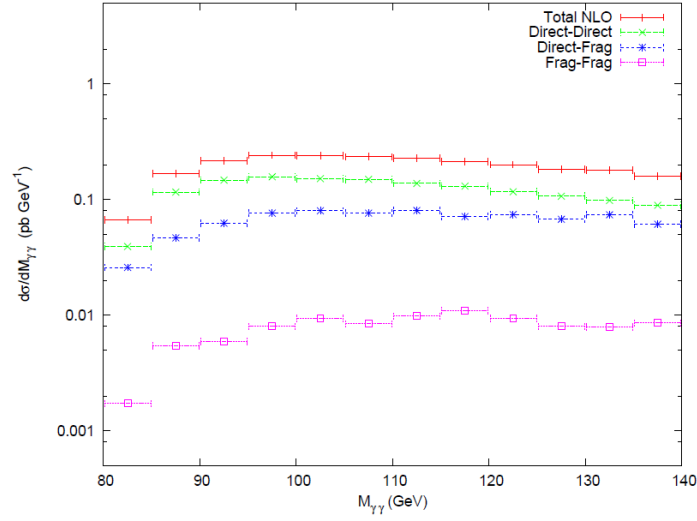
Although this calculation offers an interesting theoretical analysis of the effect of altering E_T^{max} , it also has a practical purpose, as it helps quantize the background signal for the process $H \rightarrow \gamma\gamma$ which is expected to be a dominant decay mechanism for the Higgs at the LHC. By generating a quantitative prediction for $\pi_0 - \pi_0$ and $\pi_0 - \gamma$ events, which will mimic $\gamma - \gamma$ events due to the decay of the pion, we are able to form a basis for experimentally subtracting these backgrounds. This study is developed in more detail in [10].

4.3.3 Results

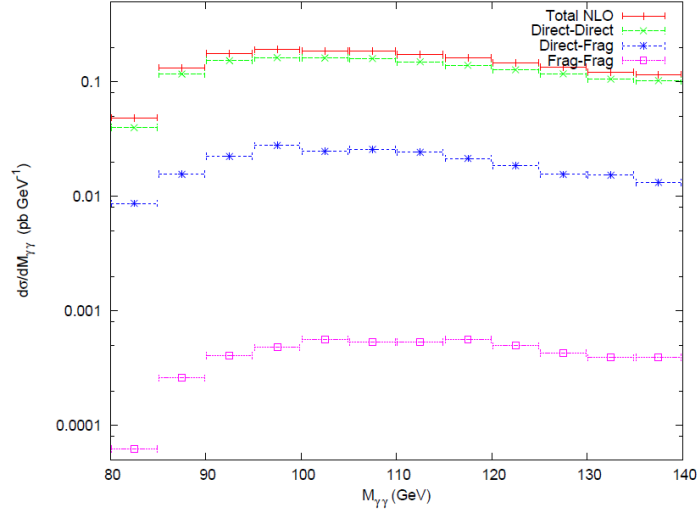
We are finally prepared to present the final results for the NLO isolated photon-pion cross-section, as calculated using Equation (3.15). Although a NLO treatment of this cross-section has already been completed in [55], this study did not fully implement the PHENIX isolation criterion, having assumed that the cross-section could be approximated by computing only the direct inclusive contribution. Although this is roughly the case in the low-mid- x_E range, the range $0.9 < x_E < 1.3$ could not be reproduced under this assumption.

Substituting the experimental isolation values $\delta = 0.3$ and $\epsilon_h = 0.1$ into our expression (3.14), we obtain $\Gamma \approx 0.003$. For this reason, we can effectively consider the isolated NLO direct contribution to be virtually identical to the inclusive contribution, given this set of parameters. As per Equation (3.8), we include the fragmentation contribution for the region $z > \frac{1}{1+\epsilon_h} = 0.91$.

We plot our results in Figure 4.5, with the same choice of scales, PDFs and FFs as in Section 4.2. Unfortunately, with the exception of the kinematic range $5GeV < p_T^\gamma < 7GeV$, the PHENIX data does not explore the high x_T kinematic range,



(a) $E_T^{max} = 100\text{GeV}$



(b) $E_T^{max} = 10\text{GeV}$

Figure 4.4: Invariant mass distribution for $\gamma - \gamma$ pairs in the $80 - 140\text{GeV}$ range at $\sqrt{s} = 14\text{TeV}$, with isolation criteria $R = 0.4$ and varying E_T^{max} .

which is primarily where the isolation method used would be tested. Nevertheless, in Figure 4.5a, we are able to see that including the fragmentation contribution does help describe data in this kinematic region, which was uninhabited in our LO plot 4.1a. In addition, for Figures 4.5b and 4.5c, the shape of the theoretical distribution fits the data more closely than in our LO calculation.

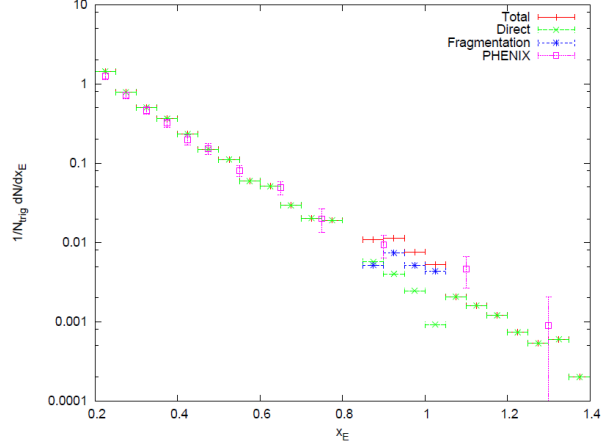
In Figure 4.6, we have also plotted the analogous result for the LHC, for the p_T^γ bin given by $85 < p_T^\gamma < 120 GeV$. As we'll discuss in the following section, it is principally in higher- p_T bins such as this one that we are interested when comparing γ -hadron spectra in $p + p$ versus nuclear collisions. This is due to the fact that jet resolution is often only possible in nuclear collisions for $p_T^{jet} > 50 GeV$ [70].

Additionally, in these p_T ranges we expect that our plots reproduce experimental data to an even greater accuracy than in the case of the PHENIX data, since the aforementioned initial-state “intrinsic” k_T effect is now trivial compared to the energies of the outgoing particles.

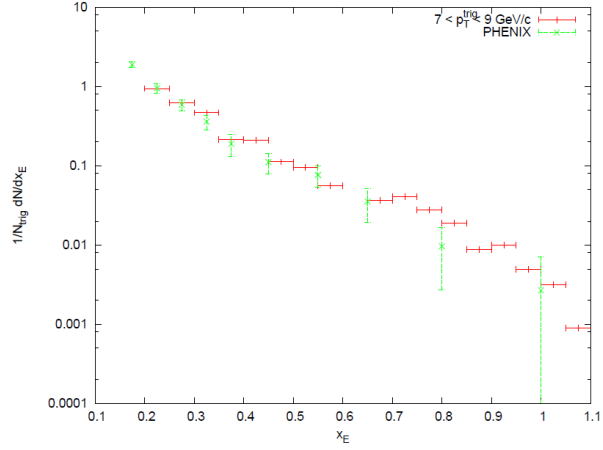
4.4 Applications to Nucleus-Nucleus Collisions

One of the most important results in modern nuclear theory is the prediction of the formation of a state of hot dense matter, the quark-gluon plasma (QGP), at high enough temperatures or energy densities [6]. The existence of this medium has been experimentally corroborated with various results from PHENIX [7]. Observables such as the cross-sections of emitted photons and hadrons serve as important probes of the QGP, as they reveal information about the temperature and energy density of the medium, which does not exist long enough to be probed by external means. The task is not entirely simple, however. Photons, for instance, are produced through a plethora of mechanisms : initial hard processes, fragmentation of hard partons, jet-medium interactions, thermal processes, and meson decay. Separating out these various signatures requires precise theoretical predictions for each signature individually. Accordingly, a large part of the recent heavy-ion programme at RHIC has been centered on establishing very good control on the so-called “baseline” measurements obtained in $p + p$ collisions.[71, 72, 73]

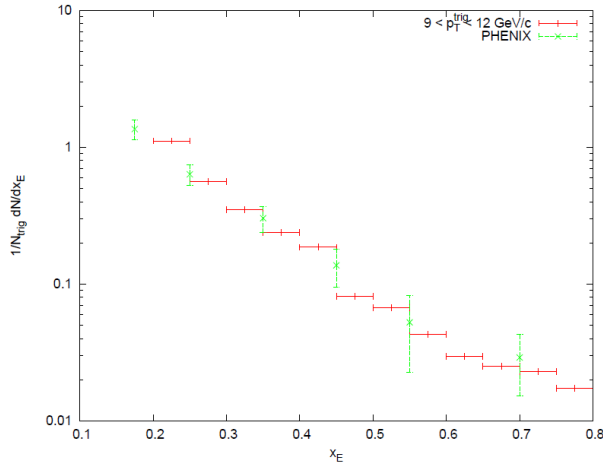
In particular, early results from RHIC [13, 14] showed a clear suppression of



(a) $5 < p_T^{trig} < 7 \text{ GeV}/c$



(b) $7 < p_T^{trig} < 9 \text{ GeV}/c$



(c) $9 < p_T^{trig} < 12 \text{ GeV}/c$

Figure 4.5: The NLO away-side charged hadron yield per isolated photon trigger as a function of x_E for the ranges $5 < p_T^{trig} < 7 \text{ GeV}/c$, $7 < p_T^{trig} < 9 \text{ GeV}/c$, and $9 < p_T^{trig} < 12 \text{ GeV}/c$. The data points and error bars are taken from PHENIX [66] and the histograms are calculated using NLO pQCD.

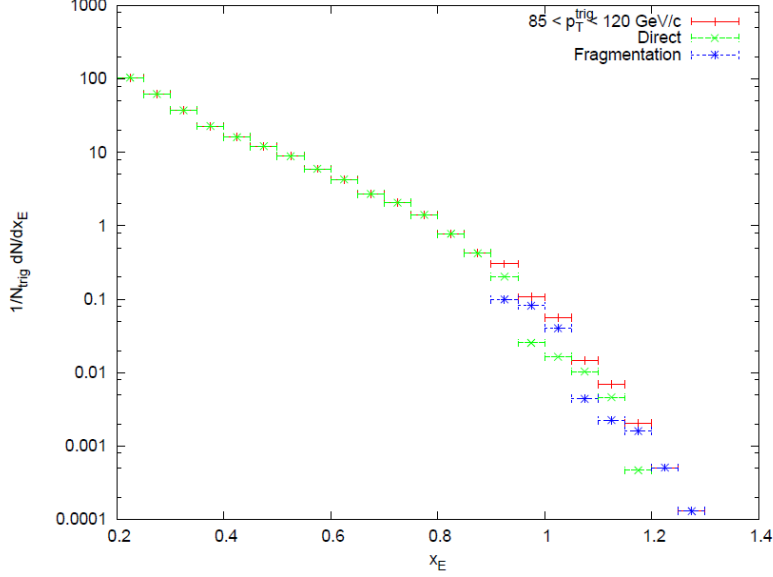


Figure 4.6: The NLO away-side charged hadron yield per isolated photon trigger as a function of x_E for the range $85 < p_T^{trig} < 120 \text{ GeV}/c$ at LHC energies. The data is calculated using isolated NLO pQCD.

high- p_T hadrons in Au + Au collisions with respect to $p + p$ collisions, the result known as “jet quenching” produced via interactions between the hard partons and the surrounding color-charged medium. This result has typically been characterized by the so-called nuclear modification variable R_{AA} for a given particle type h , defined by :

$$R_{AA}^h = \frac{1}{N_{coll}} \frac{d^2 N_{AA}^h / dp_t dy}{d^2 N_{pp}^h / dp_t dy} \quad (4.5)$$

Here, N_{coll} is a normalizing factor which is equal to the expected number of binary collisions occurring within the nuclear collision. As shown in Figure 4.7, taken from an early PHENIX publication [14], the R_{AA} for neutral pions in central collisions is approximately 0.2-0.4 in the observed p_T range. Meanwhile, in peripheral collisions, such a suppression is not apparent. In the case of photons, it has been observed that there is virtually no suppression for any centrality class [12] : we can conclude that the observed jet quenching only applies to color-charged particles, supporting the theory that this effect is due to interactions with a color-charged medium.

While R_{AA} is useful in qualitatively establishing the existence of the thermal

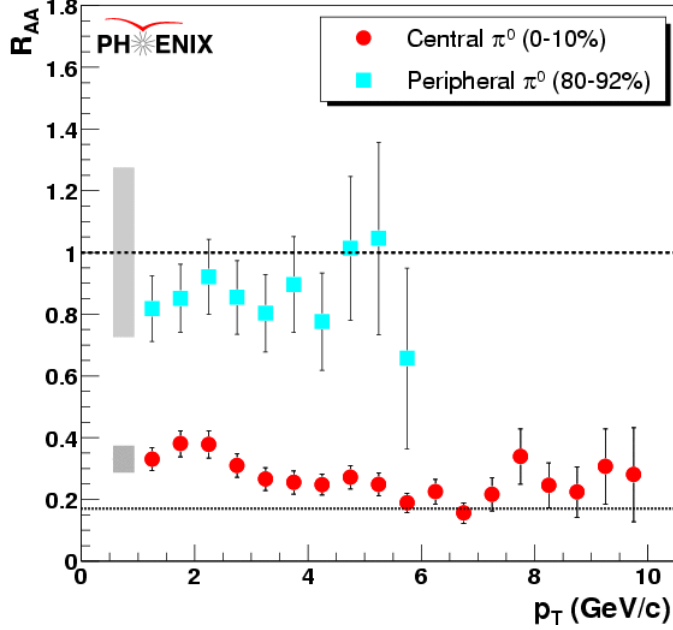


Figure 4.7: High- p_T pion R_{AA} in Au+Au collisions, as measured by PHENIX.[14]

medium, we can see that in certain respects it is not a very “differential” observable. In fact, as shown in Figure 4.8, taken from [74], there are a multitude of various models with very different jet energy loss mechanisms that all predict approximately the same values for R_{AA} . Ideally, what we would prefer to have is the specific re-distribution in phase space of a given particle species after having interacted with the medium, which can be obtained by comparing the vacuum FF to the medium-modified FF.

This is not a simple task, though, since this would require a measurement of the jet energy profile in the medium, which is done by experimentally summing all the hadrons falling within a certain jet cone radius. In nuclear collisions, these jet reconstruction techniques simply do not work at energies below 50GeV , as a result of the high background of particles created as a result of medium interactions.[70]

As shown in Section 2.6, at LO (i.e.: in $2 \rightarrow 2$ processes), two final-state partons will have equal and opposite momenta as they emerge from the collision. This means that, at LO, if we are able to observe a final-state photon-hadron pair, the photon will exactly determine the initial momentum of the parton from which the hadron fragmented, and correspondingly we can observe very specifically how the phase space of outgoing jets is modified in the medium – in effect, a “medium-

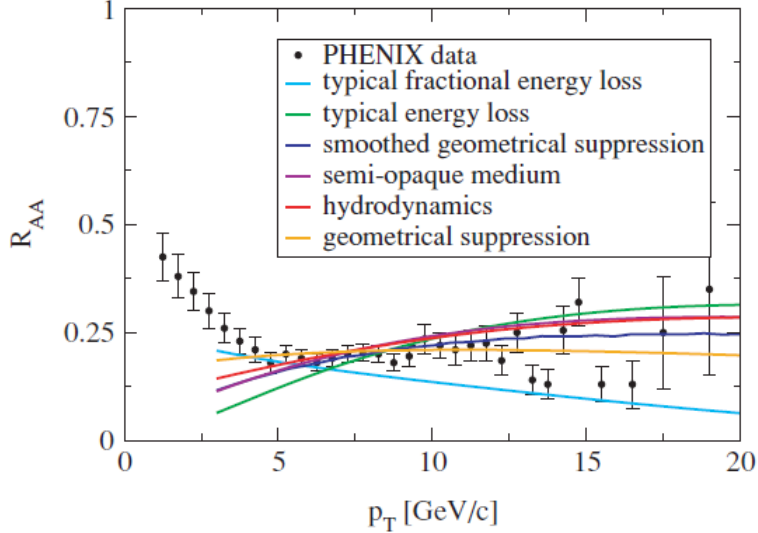


Figure 4.8: High- p_T pion R_{AA} in Au+Au collisions. The diagram is taken from [74].

modified fragmentation function”. In reality, we know that NLO effects form a significant contribution, but our newly-defined x_E should correspond precisely to the momentum fraction of the hadron with respect to the jet from which it fragments at NLO. This is exactly the variable with respect to which we should be computing the hadron’s FF.

In this way, a new nuclear modification factor I_{AA} can be defined as the scaled ratio of the γ -triggered FF in nuclear collisions with respect to $p+p$ collisions. For a given range in p_T^γ , we can write this as:

$$I_{AA}(z, \phi) \equiv \frac{P_{AA}(z, \phi)}{P_{pp}(z)} \quad (4.6)$$

In this case, $P_{pp}(z)$ is simply the number of γ -h pairs plotted as a function of z , normalized by the total number of γ ’s observed – this is in fact the quantity we have already plotted for various p_T bins in Figure 4.5 for RHIC and Figure 4.6 for the LHC. Accordingly, an experimental measurement of I_{AA} corresponds to a measurement of the medium-modified FF, and hence to a measurement of the redistribution of photon-tagged hadrons in phase space due to jet quenching.

Ultimately, this provides yet another example of the use of measuring photons in high-energy collisions. Given that experimental detectors are currently refined enough to detect correlated pairs of particles, it seems like a given that these

should be measured extensively to complement single-particle spectra. In addition, the huge backgrounds that originate in nuclear collisions suggest that those calculations over which we *do* have control – higher-order direct and fragmentation γ spectra, in this case – should be computed with the greatest level of precision possible.

Chapter 5

Conclusion

Cross-sections for both single-particle cross sections and photon-hadron cross sections have been computed up to NLO in α_s , with results broadly matching the current available experimental data from experiments at both RHIC and LHC. In particular, we have examined in detail the role of photons in hadronic collisions, and the physics which describes their various modes of production.

In Chapter 2, we presented a broad review of the theoretical ideas needed to perform cross-section computations at both LO and NLO. In particular, we saw how collinear divergences in higher order Feynman diagrams necessitated the introduction of PDFs and FFs which could absorb the non-perturbative pieces in the computation. After introducing the S-Matrix formalism and the running of α_s , we were able to simplify the kinematics in our expressions to obtain final forms for our single-particle and multi-particle spectra.

In Chapter 3, this formalism was applied in the case of single-photon and single-pion production at RHIC and LHC energies, with wide agreement with experimental results from PHENIX and CMS data respectively. A comparison between LO and NLO computations in each case showed the substantive corrections that resulted in the latter case. In addition, we were able to briefly examine the effect of altering our factorization energy scales, as well as the theoretical modifications needed in the presence of γ isolation cuts.

Chapter 4 allowed us to extend our formalism to the case of two-particle correlations. In particular, we examined the spectrum of charged hadrons tagged with photons as compared to PHENIX data, and found a remarkable agreement. Again

effects due to isolation needed to be taken into account to accurately reproduce the data. It was found that only by including effects from fragmentation and from NLO processes that we could explain the cross-section in certain kinematic regions for which no LO component existed.

It's perhaps not surprising that it has taken such a long time for both theoretical and experimental techniques to be sufficiently refined so that we have a high-precision framework in which to test predictions of pQCD. On the side of theory, one is forced to admit that, due to the asymptotically free nature of the $SU(3)$ theory, there is a fundamental barrier to making predictions at the same level of precision as in QED. Though at high energies we are in principle able to use perturbation theory, and at low energy, effective theories give reliable predictions, the normal techniques simply cannot be applied in the Λ_{QCD} range. On top of it, the fact that we observe bound states rather than free quarks means that every computation we make that we wish to compare with experiment *must deal with long distance non-perturbative physics*. It is as if these two fundamental properties of QCD – asymptotic freedom and color confinement – are working hand in hand to obscure reality from us, and to diminish the predictive power of our theory.

Though the factorization theorem salvages this somewhat, we are still forced to use distribution functions parameterized by experimental data, and introduce unphysical scales into our problem, resulting in an inherent source of theoretical uncertainty. On the other hand, there has not yet been observed any contradiction between theory and experiment, so that pQCD seems indeed to be the correct theory of the strong interaction at high energies. In addition, these issues have resulted in the development of a rich theoretical basis for non-perturbative calculations, including lattice methods and, more recently, methods related to the AdS/CFT correspondence.

For the next couple of decades, data from the LHC and other operating colliders should provide a wealth of opportunities to continue testing the Standard Model as well as models containing new physics. There is still much work to be done – we are approaching the threshold of what it is possible to engineer, so that soon entirely new experimental and theoretical methods may be needed to continue making progress. Optimistically, one can construct an analogy with the state of physics as it was at the end of the 19th century, when it was believed that almost

everything “had been done.” Now, after over a century of relativity, quantum mechanics, and all the ensuing developments, we know that the physical world is far richer and more subtle than we ever could have imagined. It may be that we just need a few new creative, paradigm-altering ideas to keep us moving on the road forward.

Appendix A

QCD Feynman Rules

In this appendix, we briefly list the Feynman rules used in computations in the thesis. The conventions are such that Roman letters a and b refer to color indices in the adjoint representation, i and j are color indices in the fundamental representation, f refers to flavor indices, and Greek letters μ and ν refer to the Lorentz structure of the expressions. The forms of the propagators and the vertices are obtained using the QCD Lagrangian, given by [75, 22]:

$$\mathcal{L}_{QCD} = -\frac{1}{4}F_{\mu\nu}^a F^{\mu\nu a} + \psi_{f,i}(i\gamma^\mu \mathcal{D}_{\mu,ij} - m_f \delta_{ij})\psi_{f,j} \quad (\text{A.1})$$

Here, $F_{\mu\nu}^a \equiv \partial_\mu A_\nu^a - \partial_\nu A_\mu^a - gf_{bc}^a A_{\mu,b} A_{\nu,c}$ is the field tensor for the gluon field A_μ^a , and $\mathcal{D}_{\mu,ij} \equiv \partial_\mu \delta_{ij} + ig(t_a)_{ij}$ is the relevant covariant derivative, which acts on the quark fields ψ_f . The set of matrices t_a must satisfy the Lie algebra binary operation:

$$[t_a, t_b] = if_{abc} t_c \quad (\text{A.2})$$

where f_{abc} are the structure constants of the Lie algebra. For QCD, described by the Lie group $SU(3)$ [22, 76], the range of the sum over color indices is given by $i, j = 1, 2, 3$ and $a, b = 1, \dots, 8$. It is a simple matter to verify that (A.1) is gauge invariant under the relevant group transformations. Because of the difficulty in quantizing a gauge-invariant Lagrangian, it is typical to add a “gauge-fixing” term, conventionally given by:

$$\mathcal{L}_{gauge} = -\frac{1}{2\xi}(\partial_\mu A_a^\mu)(\partial_\nu A_a^\nu) \quad (\text{A.3})$$

Furthermore, now having fixed ourselves in the so-called *covariant gauge*, we also need to introduce new “ghost” fields c_a and \bar{c}_a to preserve the unitarity of the scattering matrix in QCD. These additional terms in the Lagrangian take the form:

$$\mathcal{L}_{ghost} = (\partial_\mu \bar{c}_a)(\partial^\mu \delta_{ad} - gf_{abd}A_b^\mu)c_d \quad (\text{A.4})$$

Taking into account all of the interaction terms in (A.1), (A.3) and (A.4), we see that there must be vertices corresponding to the $\bar{q}gq$, ggg , $gggg$, and $\bar{c}gc$ terms. We list the Feynman diagrams for these interactions in Figure A.2, as well as all of the particle propagators in Figure A.1.

We note that, in addition to the listed Feynman rules, there is another similar set of diagrams not listed that arise from the renormalization counterterms in the renormalized Lagrangian. These can be found, for example, in [22].

Finally, we will also need one additional diagram from QED, namely that of the quark-photon interaction, obtained from the QED Lagrangian:

$$\mathcal{L}_{QED} = -\frac{1}{4}F_{\mu\nu}F^{\mu\nu} + \sum_f \psi_f(i\gamma^\mu D_\mu - m_f)\psi_f \quad (\text{A.5})$$

where $F_{\mu\nu} \equiv \partial_\mu A_\nu - \partial_\nu A_\mu$ and $D_\mu \equiv \partial_\mu - ieA_\mu$. Once again, contained in our covariant derivative is the term which couples the quark fields to the electromagnetic field, whose diagrammatic representation is given in Figure A.3. Incoming and outgoing fermionic particles are given by the Dirac wavefunctions $u(p, s)$ and $\bar{u}(p, s)$ respectively, and incoming and outgoing antiparticles are given by $\bar{v}(p, s)$ and $v(p, s)$ respectively. Incoming and outgoing vector particles are given by the polarization tensor wavefunctions $\epsilon_\mu(k, \lambda)$ and $\epsilon_\mu^*(k, \lambda)$.

The prescription for computing a matrix element is : 1. Multiply all of the relevant expressions for the propagators, vertices, and external legs, taking care to uniquely assign all momenta, color, spin, and flavor indices; 2. In the case of higher-order diagrams, integrate over undetermined loop momenta; 3. Sum all diagrams containing the initial and final states in question. Under this prescription, one need not worry about momentum conservation, which is dealt with entirely within the relevant delta functions in the expression for the cross-section (See Section 2.2).

$$= -ig\gamma^\mu \times \delta_f^{f'} \times (t^a)_i^j$$

(a) Quark-gluon vertex

$$= -gf^{abc} [g^{\alpha\beta}(k_1 - k_2)^\gamma + g^{\beta\gamma}(k_2 - k_3)^\alpha + g^{\gamma\alpha}(k_3 - k_1)^\beta]$$

(b) Three-gluon vertex

$$= -ig^2 \begin{bmatrix} f^{abe} f^{cde} (g^{\alpha\gamma} g^{\beta\delta} - g^{\alpha\delta} g^{\beta\gamma}) \\ + f^{ace} f^{bde} (g^{\alpha\beta} g^{\gamma\delta} - g^{\alpha\delta} g^{\gamma\beta}) \\ + f^{ade} f^{bce} (g^{\alpha\beta} g^{\delta\gamma} - g^{\alpha\gamma} g^{\delta\beta}) \end{bmatrix}$$

(c) Four-gluon vertex

$$= -gf^{abc} p'^\mu$$

(d) Ghost-gluon vertex

Figure A.2: Vertex rules in QCD

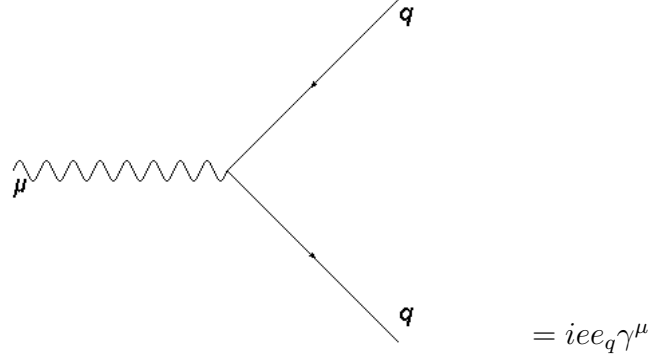


Figure A.3: Quark-photon vertex

$$\begin{aligned}
 \text{Tr}(\mathbf{1}) &= 4 & \text{Tr}(\gamma_{\mu_1} \dots \gamma_{\mu_{2n-1}}) &= 0 \quad n \in \mathbb{N} \\
 \text{Tr}(\gamma_{\mu} \gamma_{\nu}) &= 4\eta_{\mu\nu} & \text{Tr}(\gamma_{\mu} \gamma_{\nu} \gamma_{\rho} \gamma_{\sigma}) &= 4(\eta_{\mu\nu} \eta_{\rho\sigma} + \eta_{\mu\sigma} \eta_{\nu\rho} - \eta_{\mu\rho} \eta_{\nu\sigma}) \quad (\text{A.9})
 \end{aligned}$$

In particular, we use the d -dimensional expressions in the case of higher-order diagrams for which dimensional renormalization is prescribed. For LO diagrams, it is sufficient to use $d = 4$.

The final step in evaluating the pQCD squared matrix elements involves computing the so-called “color factor” for the process, for which one needs to evaluate products of the $SU(3)$ group generators t_a . For the color transformations of quarks, these are represented by the Gell-Mann matrices λ_i , $i = 1, \dots, 8$, a list of which can be found in [18], along with commonly applied mathematical identities that relate them to one another. The identities used in Chapter 2 are given by:

$$\text{Tr}(t^a t^b) = \frac{1}{2} \delta^{ab} \quad (t^a)_{ik} (t^a)_{lj} = \frac{1}{2} \delta_{ij} \delta_{lk} - \frac{1}{6} \delta_{ik} \delta_{lj} \quad (\text{A.10})$$

Although this account has been very cursory, the rules and identities here should be sufficient for the beginning reader to follow along with the computations in the thesis. Further details can be found in [16, 17, 18, 19, 21].

Bibliography

- [1] S. Weinberg, Phys. Rev. Lett. **19**, 1264 (1967).
- [2] A. Salam, *Elementary Particle Theory*, Almqvist and Forlag AB, Stockholm, 1969.
- [3] S. L. Glashow, J. Iliopoulos, and L. Maiani, Phys. Rev. **D2**, 1285 (1970).
- [4] M. Gell-Mann, Phys. Lett. **8**, 214 (1964).
- [5] G. Zweig, An SU(3) model for strong interaction symmetry and its breaking, 1964.
- [6] F. Karsch, Nuclear Physics **A**, 199 (2002).
- [7] K. Adcox et al., Nucl. Phys. A **757** (2005).
- [8] P. Aurenche, R. Baier, M. Fontannaz, J. F. Owens, and M. Werlen, Phys. Rev. D **39**, 3275 (1989).
- [9] M. Werlen et al., Phys. Lett. B **452**, 201 (1999).
- [10] T. Binoth, J.-P. Guillet, E. Pilon, and M. Werlen, Eur. Phys. J. C **22** (2002).
- [11] X.-N. Wang, Z. Huang, and I. Sarcevic, Phys. Rev. Lett. **77**, 231 (1996).
- [12] S. S. Adler et al., Phys. Rev. Lett. **94** (2005).
- [13] K. Adcox et al., Phys. Rev. Lett. **88** (2001).
- [14] S. S. Adler et al., Phys. Rev. Lett. **91** (2003).
- [15] K. J. Eskola, H. Honkanen, H. Niemi, P. V. Ruuskanen, and S. S. Räsänen, Phys. Rev. C **72**, 044904 (2005).

- [16] M. Peskin and D. Schroeder, *Introduction to Quantum Field Theory*, Perseus Books Group, New York, NY, 1995.
- [17] C. Burgess and G. D. Moore, *The Standard Model : A Primer*, Cambridge University Press, London, 2006.
- [18] R. D. Field, *Applications of Perturbative QCD*, Addison Wesley Publishing Company, Reading, MA, 1989.
- [19] G. Sterman et al., *Rev. Mod. Phys.* **67**, 157 (1995).
- [20] J. C. Collins, D. E. Soper, and G. F. Sterman, *Adv. Ser. Direct. High Energy Phys.* **5**, 1 (1988).
- [21] J. M. Campbell, J. W. Huston, and J. Stirling, *Rep. Prog. Phys.* **70**, 89 (2007).
- [22] D. Gross and F. Wilczek, *Phys. Rev. D.* **8**, 3633 (1973).
- [23] H. D. Politzer, *Phys. Rev. Lett.* **30**, 1346 (1973).
- [24] R. P. Feynman, *Phys. Rev. Lett.* **23**, 1415 (1969).
- [25] R. P. Feynman, *Photon-hadron interactions*, Addison-Wesley, 1972.
- [26] S. D. Drell and T.-M. Yan, *Ann. Phys.* **66**, 578 (1971).
- [27] P. Aurenche and J. Lindfors, *Nucl. Phys. B* **168**, 296 (1980).
- [28] M. Nowak and M. Praszalowicz, *Z. Phys. C* **17**, 249 (1983).
- [29] A. P. Contogouris, R. Gaskell, and L. Marleau, *Phys. Rev. D* **22**, 1109 (1980).
- [30] G. 't Hooft, *Nucl. Phys. B* **33**, 173 (1971).
- [31] B. W. Lee and J. Zinn-Justin, *Phys. Rev. D* **5**, 3121 (1972).
- [32] B. W. Lee and J. Zinn-Justin, *Phys. Rev. D* **7**, 1049 (1973).
- [33] G. M. Prosperi, M. Raciti, and C. Simolo, *Prog. Part. & Nucl. Phys.* **58**, 387 (2007).
- [34] J. C. Collins and W.-K. Tung, *Nucl. Phys.* **B278**, 934 (1986).

- [35] P. Aurenche, M. Fontannaz, J. P. Guillet, E. Pilon, and M. Werlen, Phys. Rev. D **73** (2006).
- [36] S. Catani, M. Fontannaz, J. Guillet, and E. Pilon, JHEP **05** (2002).
- [37] PDG Group, Color & Confinement, <http://pdg.web.cern.ch/pdg/cpep/color.html>.
- [38] S. B. Libby and G. Sterman, Phys. Rev. D **18**, 3252 (1978).
- [39] J. C. Collins, *Renormalization: An Introduction to Renormalization, the Renormalization Group, and the Operator Product Expansion*, Cambridge University Press, London, 1984.
- [40] J. F. Owens, Rev. Mod. Phys. **59**, 465 (1987).
- [41] G. Altarelli and G. Parisi, Nucl. Phys. B **126**, 298 (1977).
- [42] H. Lai et al., Eur. Phys. J. C **12**, 375 (2000).
- [43] A. D. Martin, W. J. Stirling, R. S. Thorne, and G. Watt, Eur. Phys. J. **63**, 189 (2009).
- [44] H.-L. Lai et al., Phys. Rev. D **82** (2010).
- [45] D. E. Soper, Nucl. Phys. B **53**, 69 (1997).
- [46] J. Binnewies, B. A. Kniehl, and G. Kramer, Z. Phys. C **65**, 471 (1995).
- [47] B. A. Kniehl, G. Kramer, and B. Potter, Nucl. Phys. B **582**, 514 (2000).
- [48] L. Bourhis, M. Fontannaz, and J. P. Guillet, Eur. Phys. J. C **2**, 529 (1998).
- [49] V. N. Gribov and L. N. Lipatov, Sov. J. Nucl. Phys. **15**, 438 (1972).
- [50] Y. L. Dokshitzer, Sov. Phys. JETP **46**, 641 (1977).
- [51] J. F. Owens, Phys. Lett. B **76**, 85 (1978).
- [52] T. Uematsu, Phys. Lett. B **79**, 97 (1978).
- [53] W. Celmaster and D. Sivers, Phys. Rev. D **23**, 227 (1981).
- [54] P. M. Stevenson, Phys. Lett. **B100**, 61 (1981).

- [55] H. Zhang, J. F. Owens, E. Wang, and X. Wang, Phys. Rev. Lett **103** (2009).
- [56] Y. Mao et al., Eur. Phys. J. C **57**, 613 (2008).
- [57] M. Klasen, Rev. Mod. Phys. **74**, 1221 (2002).
- [58] S. S. Adler et al., Phys Rev. Lett. **98** (2007).
- [59] P. Aurenche, R. Baier, A. Douiri, M. Fontannaz, and D. Schiff, Phys. Lett. B **140**, 87 (1984).
- [60] S. Frixione, Phys. Lett. B **429**, 369 (1998).
- [61] E. Berger and J. Qiu, Phys. Rev. D **44**, 2002 (1991).
- [62] J. Guillet, (Personal communication, Mar. 2011).
- [63] F. E. Low, Phys. Rev. **110**, 974 (1958).
- [64] G. McKeon, Phys. Rev. D **15**, 3668 (1977).
- [65] V. Khachatryan et al., Phys. Rev. Lett. **106** (2011).
- [66] S. S. Adler et al., Phys Rev. Lett. **91** (2003).
- [67] P. Darriulat et al., Nucl. Phys. B **107**, 429 (1976).
- [68] R. P. Feynman, R. D. Field, and G. C. Fox, Nucl. Phys. B **128**, 1 (1977).
- [69] G. Altarelli, R. K. Ellis, M. Greco, and G. Martinelli, Nucl. Phys. B **246**, 12 (1984).
- [70] A. Morsch, Nucl. Phys. A **783**, 427 (2007).
- [71] A. Adare et al., Phys. Rev. D **82** (2010).
- [72] A. Adare et al., Phys. Rev. D **83** (2011).
- [73] A. Adare et al., Phys. Rev. D **79** (2009).
- [74] T. Renk, Phys. Rev. C **74** (2006).
- [75] C. N. Yang and R. L. Mills, Phys. Rev. **96**, 191 (1954).
- [76] H. Fritzsch, M. Gell-Mann, and H. Leutwyler, Phys. Lett. B **47**, 365 (1973).